A three-pronged approach to predict the effect of plastic orthotropy on the formability of thin sheets subjected to dynamic biaxial stretching

K.E. N'souglo, Nicolas Jacques, J.A. Rodríguez-Martínez

A three-pronged approach to predict the effect of plastic orthotropy on the formability of thin sheets subjected to dynamic biaxial stretching

K. E. N'souglo[a], N. Jacques[b,*], J. A. Rodríguez-Martínez[a]

[a] *Department of Continuum Mechanics and Structural Analysis. University Carlos III of Madrid. Avda. de la Universidad, 30. 28911 Leganés, Madrid, Spain*

[b] *ENSTA Bretagne, CNRS UMR 6027, IRDL, 2 rue François Verny, F-29806 Brest Cedex 9, France*

Abstract

In this paper, we have investigated the effect of material orthotropy on the formability of metallic sheets subjected to dynamic biaxial stretching. For that purpose, we have devised an original three-pronged methodology which includes a linear stability analysis, a nonlinear two-zone model and finite element calculations. We have studied 5 different materials whose mechanical behavior is described with an elastic isotropic, plastic anisotropic constitutive model with yielding based on Hill (1948) criterion. The linear stability analysis and the nonlinear two-zone model are extensions of the formulations developed by Zaera et al. (2015) and Jacques (2020), respectively, to consider Hill (1948) plasticity. The finite element calculations are performed with ABAQUS/Explicit (2016) using the unit-cell model developed by Rodríguez-Martínez et al. (2017), which includes a sinusoidal spatial imperfection to favor necking localization. The predictions of the stability analysis and the two-zone model are systematically compared against the finite element results –which are considered as the reference approach to validate the theoretical models– for loading paths ranging from plane strain stretching to equibiaxial stretching, and for different strain rates ranging from 100 s^{-1} to 50000 s^{-1}. The stability analysis and the two-zone model yield the same overall trends obtained with the finite element simulations for the 5 materials investigated, and for most of the strain rates and loading paths the agreement for the necking strains is also quantitative. Notably, the differences between the finite element results and the two-zone model rarely go beyond 5%. Altogether, the results presented in this work provide new insights into the mechanisms which control dynamic formability of anisotropic metallic sheets.

Keywords:

Dynamic formability, Necking, Plastic orthotropy, Linear stability analysis, Two-zone model, Finite elements

*Corresponding author. Tel. +33 2 98 34 89 36; fax. +33 2 98 34 87 30. E-mail address: nicolas.jacques@ensta-bretagne.fr

1. Introduction

Interest of aeronautical and automotive industries in high energy rate forming (HERF) processes, such as explosive, electromagnetic and electrohydraulic forming, has been growing in recent years due to their potential to form aluminium, titanium, high-strength steel and other low formability metallic materials (Song et al., 2004). The high strain rates achieved in HERF processes in comparison to conventional quasi-static metal forming operations lead to significant changes in the constitutive behavior of the materials and give rise to inertial effects which contribute to delay necking localization and ductile fracture (Mamalis et al., 2004; Gayakwad et al., 2014).

The first experimental evidence that inertia effects improve the formability of metal sheets was most likely provided by Wood (1967), who showed that the ductility of several materials (stainless steel, vascojet tool steel, René 41 superalloy) is significantly increased during high-explosive forming operations, such as tube and dome bulging. More recently, Balanethiram and Daehn (1992) obtained the dynamic formability diagrams of Interstitial Free iron sheets with 0.84 mm thickness tested at strain rates of $\sim 10^3$ s^{-1} using electrohydraulic forming (the sheets were formed inside a conical die with 90° apex angle). The comparison with the corresponding quasi-static forming limits showed that the ductility of the specimens near plane strain increased by three times at high strain rates. Shortly after, Balanethiram and Daehn (1994) presented additional electrohydraulic experiments showing that the formability of AA 6061 and OFHC copper sheets also increases at high strain rates, suggesting that the beneficial contribution of inertial forces to the ductility of metals sheets is *both large and general* (Balanethiram and Daehn, 1994). The experiments on OFHC copper were performed using sheets of 0.34 and 0.79 mm thickness, with the thicker samples showing much greater improvement in formability at high strain rates due to the increase of inertia effects with the specimen thickness. Hence, Daehn et al. (1995) concluded that when inertial forces are at work in stabilizing necking, size effects become important.

Years later, Seth et al. (2005) investigated experimentally the dynamic formability of sheet specimens made of five different cold-rolled steels with thicknesses varying from 0.15 to 0.38 mm. The tests consisted of launching electromagnetically the steel sheets at a shaped punch at velocities of 50–220 m/s. Similarly to the experimental evidence presented by Balanethiram and Daehn (1992, 1994) for Interstitial Free iron, AA 6061 and OFHC copper, the ductility of these five steels was also dramatically increased at high strain rates as compared to the quasi-static forming limit diagrams. The experimental results reported by Golovashchenko (2007) for the electromagnetic forming of AA 6111-T4 and AA 5754 sheets into conical and v-shape dies also showed that the ductility of the electromagnetic formed samples can be ~ 2.5 times greater than under quasi-static loading. Dariani et al. (2009)

obtained the forming limit diagrams of AA 6061-T6 and 1045 steel under quasi-static and explosive loading (in the latter case the strain rate reaches $\sim 10^3$ s^{-1}). These experiments revealed that the ductility of the explosively formed specimens increases by a factor of 2.5 for AA6061-T6 and by factor of 1.6 for 1045 steel. Golovashchenko et al. (2013) investigated the dynamic formability of four different dual phase steels (DP500, DP590, DP780 and DP980) at strain rates up to $\sim 2 \cdot 10^4$ s^{-1} using electrohydraulic forming. As compared to the quasi-static case, the relative improvement in plane strain formability in electrohydraulic forming conditions was between 63% and 190%, depending on the grade of dual phase steel. Moreover, Rohatgi et al. (2014) performed electrohydraulic forming experiments which showed that the dynamic formability of AA 5182-O sheets of 1 mm thickness, relative to its corresponding quasi-static formability, increases by ~ 2.5 times and ~ 6.5 times under free-forming and when forming inside a conical die, respectively.

Theoretical investigations to rationalize the effect of inertia on neck retardation have been conducted using both linear and nonlinear analyses.

Most of the linear analyses are based on the linear perturbation theory, which evaluates the growth of an infinitesimal perturbation superimposed on the homogenous background solution of the problem at hand. Fressengeas and Molinari (1985) showed that if the perturbation grows faster than the background solution, the plastic flow is unstable and a neck-like deformation field can develop. Fressengeas and Molinari (1994) extended the plane strain linear stability analysis of Hutchinson et al. (1978b) to include inertia effects, and they showed that inertia decreases the growth rate of perturbations, slowing down necking development and enhancing material ductility. In addition, it was demonstrated that at high strain rates, unlike what happens under quasi-static loadings, there is a perturbation of finite wavelength (so-called the critical wavelength) for which the growth rate of the perturbation is maximum. This critical wavelength was used by Fressengeas and Molinari (1994) to determine the average spacing between necks in the multiple localization patterns that emerge in shaped-charge jets, and satisfactory agreement was found between theory and experimental data available in the literature. Mercier et al. (2010) extended the plane strain linear stability analysis developed by Fressengeas and Molinari (1994) to thermoviscoplastic materials to predict the critical conditions for the nucleation of necks and the spacing between necks in hemispherical shells made of copper and tantalum, and subjected to dynamic expansion at strain rates of $\sim 10^4$ s^{-1}. The stability analysis predictions were in reasonable agreement with the number of necks obtained in the experiments and showed that inertia delays the formation of necks (which indeed nucleate for strains greater than the Considère (1885) strain, see also Vaz-Romero et al. (2017)). Moreover, Zaera et al. (2015) extended the linear stability analysis

developed by Dudzinski and Molinari (1991) to consider inertia effects and study the formation of multiple necks in thin metal sheets modeled with von Mises plasticity and subjected to biaxial loading at high strain rates. Using the concept of *effective instability* introduced by Dudzinski and Molinari (1991), which states that a perturbation mode turns into a necking mode when the grow rate of the perturbation reaches a critical value, Zaera et al. (2015) used the results of the stability analysis to construct dynamic forming limit diagrams. The predictions of the stability analysis were in qualitative agreement with finite element results which showed that the average spacing between necks increases as the loading path moves away from uniaxial tension and approaches equibiaxial tension (see also Rodríguez-Martínez et al. (2017)). The stability analysis also predicted in agreement with the finite element calculations the orientation of the necking bands that form the localization pattern, which are aligned with the direction of zero stretch for loading paths between uniaxial tension and plane strain (Hill, 1952), and they are perpendicular to the principal loading direction when the loading path lies between plane strain and equibiaxial tension. In addition, the finite element calculations indicated that the formability of metal sheets increases as the loading rate increases, in agreement with the experimental evidence discussed above (see also Rodríguez-Martínez et al. (2017)).

Moreover, the nonlinear analyses are generally based on the hypothesis of Marciniak and Kuczyński (1967) that necking is initiated by an *ab initio* geometric imperfection of the specimen in the form of a thickness variation, and they are usually known as two-zone models or long-wavelength analyses (Hutchinson et al., 1978b). For instance, Fressengeas and Molinari (1985) developed a one-dimensional model based on the long-wavelength approximation including material inertia to investigate the effect of strain rate on necking localization under uniaxial tension. Despite the limitations of the model, that did not consider the multiaxial stress state that develops in a necked section, Fressengeas and Molinari (1985) succeeded to provide one of the first theoretical verifications that neck formation is delayed at high strain rates. Years later, Xue et al. (2008) formulated a dynamic two-zone analysis to investigate necking in thin plates subjected to plane strain extension. The theoretical predictions were compared against finite element simulations in which the plate was modeled as an array of unit-cells with sinusoidal periodic geometric imperfections. The calculations were performed for strain rates ranging from 100 s^{-1} to 2000 s^{-1} (but for a plate with large thickness of 20 mm, which promotes inertia effects). The two-zone analysis did a good job capturing neck retardation due to inertia effects, however, because triaxiality effects were not included in the formulation of the model (as in the one-dimensional model of Fressengeas and Molinari (1985)), short necking wavelengths were not suppressed, and the two-zone analysis failed to predict the emergence of a critical necking wavelength associated to the minimum necking strain (which determines the average spacing between necks in

multiple localization problems, as mentioned before). Very recently, Jacques (2020) developed a two-zone model that extends the work of Xue et al. (2008) to consider any arbitrary in-plane loading and includes stress triaxiality effects using Bridgman (1952) approximation to account for the hydrostatic stresses which develop inside a necked region. The predictions of the model of Jacques (2020) were validated against the dynamic forming experiments of Golovashchenko et al. (2013) and the unit-cell finite element calculations of Rodríguez-Martínez et al. (2017), who extended the computational model of Xue et al. (2008) to consider loading paths ranging from plane strain to equibiaxial tension. Excellent agreement was found between theoretical model predictions and finite element calculations, providing a definite theoretical confirmation of the stabilizing effect of inertia on neck development for different strain rates and loading paths, ranging from uniaxial tension to equibiaxial tension. The two-zone model of Jacques (2020) also succeeded to capture the decrease of the critical necking wavelength with the strain rate, and its increase as the loading path moves away from plane strain to equibiaxial tension. The increase in ductility at high strain rates predicted by the two-zone model was also found in agreement with the experimental data of Golovashchenko et al. (2013).

However, most of the theoretical works cited in this introduction were specifically formulated for isotropic materials. To the authors' knowledge, neither stability analysis nor two-zone models have been yet developed to study the influence of inertia in the dynamic formability of anisotropic metal sheets. This is an important gap in the literature, as it is known that most sheet metal products are anisotropic. Thus, in this paper, we extend the stability analysis of Zaera et al. (2015) and the two-zone model of Jacques (2020) to consider orthotropic Hill (1948) plasticity. The necking strains calculated with both theoretical models are compared to finite element calculations performed with the unit-cell model used by Rodríguez-Martínez et al. (2017), for a wide range of strain rates ranging from 100 s^{-1} to 50000 s^{-1}, and for loading paths varying from plane strain to equibiaxial tension. We consider that the loading axes are parallel to the orthotropy axes of the material. Therefore, for this range of loading paths, the orientation of the necking band is perpendicular to the principal loading direction, so that the orientation of the geometric imperfection to be included in the unit-cell finite element model is known. The stability analysis and the two-zone model predict the same overall trends obtained with the finite element calculations, and for most of the strain rates and loading paths investigated, the agreement for the necking strains is also quantitative, notably the differences between the finite element results and the two-zone model rarely go beyond 5%. Altogether, this paper presents several methodologies to predict dynamic formability diagrams for anisotropic materials, and provides additional insights into the stabilizing role of inertia on neck development for

different loading paths.

2. Constitutive framework

The mechanical behavior of the materials studied in this paper is described using an elastic isotropic, plastic anisotropic constitutive model with yielding based on Hill's criterion (Hill, 1948). The formulation of the constitutive model is outlined in Section 2.1, and the values of the parameters corresponding to the five materials investigated are given in Section 2.2.

2.1. Formulation

We consider the additive decomposition of the total rate of deformation tensor $\mathbf{d}$ into an elastic part $\mathbf{d}^e$ and a plastic part $\mathbf{d}^p$ as follows:

$$\mathbf{d} = \mathbf{d}^e + \mathbf{d}^p \tag{1}$$

The elastic part of the rate of deformation tensor is related to the rate of the stress by the following linear hypo-elastic law:

$$\overset{\triangledown}{\boldsymbol{\sigma}} = \mathbf{C} : \mathbf{d}^e \tag{2}$$

where $\overset{\triangledown}{\boldsymbol{\sigma}}$ is an objective derivative of the Cauchy stress tensor, which corresponds to the Green-Naghdi derivative in ABAQUS/Explicit (2016) (when a VUMAT user-subroutine is used), and $\mathbf{C}$ is the tensor of isotropic elastic moduli given by:

$$\mathbf{C} = 2G\mathbf{I}' + K\mathbf{1} \otimes \mathbf{1} \tag{3}$$

with $\mathbf{1}$ being the unit second-order tensor and $\mathbf{I}'$ being the unit deviatoric fourth-order tensor. Moreover G and K are the shear and bulk moduli, respectively.

The yield condition is defined as:

$$f = \bar{\sigma} - \sigma_Y = 0 \tag{4}$$

where $\bar{\sigma}$ is the effective stress associated to the Hill (1948) criterion:

$$\begin{aligned}\bar{\sigma} = \big[&(G+H)\sigma_{11}^2 + (F+H)\sigma_{22}^2 + (F+G)\sigma_{33}^2 - \\ &2H\sigma_{11}\sigma_{22} - 2F\sigma_{22}\sigma_{33} - 2G\sigma_{11}\sigma_{33} + 2N\sigma_{12}^2 + 2L\sigma_{23}^2 + 2M\sigma_{13}^2\big]^{1/2}\end{aligned} \tag{5}$$

with σ_{ij} $(i,j = 1,...,3)$ being the components of the Cauchy stress tensor in the Cartesian coordinate system (X_1, X_2, X_3) associated to the orthotropy axes (see Figs. 3 and 4). Moreover F, G, H, L, M and N are the anisotropy parameters (see Section 2.2). Note that the von Mises (1928) yield criterion is recovered if $F = G = H = 0.5$ and $L = M = N = 1.5$.

In equation (4), σ_Y is the yield stress of the material in uniaxial tension in the rolling direction, which is considered to evolve with the effective plastic strain $\bar{\varepsilon}^p$, the effective plastic strain rate $\dot{\bar{\varepsilon}}^p$ and the temperature T, according to the following power-law type relation:

$$\sigma_Y = \sigma^0 \left(\varepsilon^0 + \bar{\varepsilon}^p\right)^n \left(\frac{\dot{\bar{\varepsilon}}^p}{\dot{\varepsilon}_{ref}}\right)^m \left(\frac{T}{T_{ref}}\right)^{-\mu} \tag{6}$$

where σ^0, ε^0, n, $\dot{\varepsilon}_{ref}$, m, T_{ref} and μ are material parameters (see Section 2.2). Moreover, most of the results presented in this paper have been obtained with a rate-independent behaviour ($m = 0$) under isothermal conditions of deformation ($\beta = 0$, see equation (10)). This facilitates the identification of the specific role played by material orthotropy in the dynamic formability of metallic materials (see Section 6). The influence of strain-rate sensitivity and thermal softening is specifically discussed in Section 6.4.

The effective plastic strain is related to the effective plastic strain rate as follows:

$$\bar{\varepsilon}^p = \int_0^t \dot{\bar{\varepsilon}}^p(\tau)\mathrm{d}\tau \tag{7}$$

Assuming an associated plastic flow rule, the plastic part of the rate of deformation tensor is:

$$\mathbf{d}^p = \dot{\bar{\varepsilon}}^p \frac{\partial \bar{\sigma}}{\partial \boldsymbol{\sigma}} \tag{8}$$

where the effective plastic strain rate $\dot{\bar{\varepsilon}}^p$ is defined as:

$$\dot{\bar{\varepsilon}}^p = \left[\frac{F(d_{11}^p)^2 + G(d_{22}^p)^2 + H(d_{33}^p)^2}{FG + FH + GH} + \frac{2(d_{12}^p)^2}{N} + \frac{2(d_{23}^p)^2}{L} + \frac{2(d_{13}^p)^2}{M} \right]^{1/2} \tag{9}$$

with d_{ij}^p $(i, j = 1, ..., 3)$ being the components of the plastic part of the rate of deformation tensor in the Cartesian coordinate system (X_1, X_2, X_3) associated to the orthotropy axes (see Figs. 3 and 4).

Moreover, assuming adiabatic conditions of deformation (no heat flux) and considering that plastic work is the only source of heating, the evolution of temperature is given by:

$$\dot{T} = \beta \frac{\bar{\sigma} \dot{\bar{\varepsilon}}^p}{\rho C_p} \tag{10}$$

where β is the Taylor-Quinney coefficient, ρ is the current material density and C_p is the specific heat.

The formulation of the constitutive behaviour is completed with the Kuhn–Tucker loading–unloading conditions:

$$\dot{\bar{\varepsilon}}^p \geqslant 0, \qquad f \leqslant 0, \qquad \dot{\bar{\varepsilon}}^p f = 0 \tag{11}$$

and the consistency condition during plastic loading:

$$\dot{f} = 0 \tag{12}$$

Hill's model (Hill, 1948) highlights due to its simplicity, versatility and easy calibration procedure; so that 70 years after its publication, the criterion of Hill (1948) still is widely used to describe the directionality of plastic properties of metallic materials in scientific and technological applications (Padmanabhan et al., 2009; Koubaa et al., 2017; Korkolis et al., 2018; Greco et al., 2018; Baral et al., 2018). On the other hand, we are aware that Hill's model, which is quadratic in stresses and contains only six independent parameters to describe the state of anisotropy (see equation (5)), cannot capture complex anisotropic behaviors observed for some materials (Hu, 2007; Banabic, 2010). Thus, in future works, we will extend the three approaches developed in this paper to consider more advanced yield criteria specifically developed to model the mechanical response of highly textured metallic materials which exhibit complex plastic anisotropy (e.g. the models of Karafillis and Boyce (1993), Bron and Besson (2004), Cazacu et al. (2006) and Aretz and Barlat (2013)).

2.2. Materials investigated

We investigate 5 different materials denoted as Material 1, ..., Material 5. Materials 1 and 2 are *model materials* with elastic properties and initial density representative of steel, and anisotropy parameters and parameters of the yield stress in the rolling direction that have been specifically tailored to bring to light the roles of inertia and orthotropy in dynamic formability. Materials 3, 4 and 5 are actual materials, namely, TRIP-780 steel, aluminium alloy 5182-O and aluminium alloy 6016-T4. These three materials are widely used in different industrial sectors and engineering applications, and their sheet products are often used in forming operations (Butuc et al., 2002; Li et al., 2010; Ju et al., 2015; Zhou et al., 2018). The values of the parameters corresponding to Materials $1, ..., 5$ are shown in Table 1. Note that all five materials show full in-plane anisotropy and through thickness isotropy. We are aware that using the simple power-law type relation given in equation (6) to describe the yield stress of the materials investigated in this work is a strong assumption (see the works of Zerilli and Armstrong (1987), Nemat-Nasser and Li (1998) and Rusinek and Klepaczko (2001) where more advanced constitutive relations are developed), especially for TRIP-780 steel, for which the martensitic transformation that occurs at large strains may lead to stress-strain curves with sigmoidal shape (see the works of Tomita and Iwamoto (1995), Iwamoto et al. (1998) and Choi et al. (2010)), which cannot be modeled by equation (6). Nevertheless, using a simple power-law type relation limits the number of material parameters, which facilitates to perform the parametric analysis carried out in Section 6, and it helps in the interpretation of results.

Fig. 1 shows the normalized plane stress theoretical yield loci for biaxial loading conditions, σ_I/σ_Y versus

Symbol	Property and units	Material 1	Material 2	Material 3 TRIP-780 steel	Material 4 AA 5182-O	Material 5 AA 6016-T4
ρ^0	Initial density (kg/m^3)	7850	7850	7850	2700	2700
G	Elastic shear modulus (GPa), Eq. (3)	75.19	75.19	75.19	25.94	25.94
K	Bulk modulus (GPa), Eq. (3)	196.1	196.1	196.1	67.65	67.65
C_p	Specific heat (J/Kg K), Eq. (10)	460	460	460	910	910
β	Taylor-Quinney coefficient, Eq. (10)	0, 0.9	0	0	0	0
σ^0	Yield stress parameter (MPa), Eq. (6)	300	300	1351	585.2	417.85
ε^0	Yield stress parameter, Eq. (6)	0.023	0.023	0.007	0.005	0.01
n	Yield stress parameter, Eq. (6)	0.12	0.12	0.169	0.3232	0.245
m	Yield stress parameter, Eq. (6)	0, 0.01, 0.02	0	0	0	0
$\dot{\varepsilon}_{ref}$	Yield stress parameter (1/s), Eq. (6)	1000	1000	1000	1000	1000
μ	Yield stress parameter, Eq. (6)	0.5	0	0	0	0
T_{ref}	Yield stress parameter (K), Eq. (6)	300	300	300	300	300
F	Orthotropy parameter, Eqs. (5) and (9)	0.276	0.208	0.391	0.472	0.729
G	Orthotropy parameter, Eqs. (5) and (9)	0.332	0.625	0.532	0.609	0.556
H	Orthotropy parameter, Eqs. (5) and (9)	0.668	0.375	0.468	0.391	0.444
N	Orthotropy parameter, Eqs. (5) and (9)	1.229	1.250	1.386	1.663	1.194
L	Orthotropy parameter, Eqs. (5) and (9)	1.5	1.5	1.5	1.5	1.5
M	Orthotropy parameter, Eqs. (5) and (9)	1.5	1.5	1.5	1.5	1.5

Table 1: Values of the parameters for Material 1, ..., Material 5. Numerical values of initial density, elastic constants, physical constants, parameters of the yield stress in the rolling direction and plastic orthotropy parameters. Initial density, elastic properties and physical constants of Materials 1 and 2 (*model materials*) are representative of steel and the parameters of the yield stress in the rolling direction and the plastic orthotropy parameters have been specifically tailored to bring out the roles of inertia and orthotropy in dynamic formability (see Section 6). The parameters of Materials 3, 4 and 5 which correspond to TRIP-780 steel, AA 5182-O and AA 6016-T4, respectively, are taken from Panich et al. (2013), Banabic et al. (2004) and Butuc et al. (2003).

σ_{II}/σ_Y, where σ_I and σ_{II} are the components of the Cauchy stress tensor in the rolling and transverse directions, respectively, for the five materials considered in this paper. We only show the tension-tension quadrant because all the calculations presented in Section 6 correspond to $\sigma_I > 0$ and $\sigma_{II} > 0$. Specifically, we investigate the loading cases that lie within the yellow markers that correspond to plane strain tension.

Fig. 1a compares the results for Material 1 and Material 2 with the von Mises material. For Material 1 the yield locus is exterior to the von Mises ellipsoid, showing large differences near equibiaxial tension which are gradually reduced as the $\sigma_I/\sigma_Y = 0$ axis is approached. The curvature of the yield locus of Material 1 near equibiaxial tension is significantly greater than for the von Mises material. For Material 2, the yield locus intersects to the von Mises ellipsoid, so that the locus of Material 2 turns from being slightly interior to the von Mises ellipsoid to being exterior and showing important differences in the sector $\sigma_{II} > \sigma_I$. Note also that the yield loci of Materials 1 and 2 intersect at $\sigma_I/\sigma_Y \approx 0.87$, such that for $\sigma_I/\sigma_Y \gtrsim 0.87$ the yield locus of Material 1 is exterior to Material 2, and vice versa for $\sigma_I/\sigma_Y \lesssim 0.87$.

Fig. 1b compares the results for TRIP-780 steel, AA 5182-O and AA 6016-T4 with the von Mises material. The yield loci of TRIP-780 steel and AA 6016-T4 are exterior and interior to the von Mises ellipsoid, respectively, with increasing differences near $\sigma_I/\sigma_Y = 0$. Moreover, the yield loci of von Mises material and AA 5182-O intersect at $\sigma_I/\sigma_Y \approx 0.72$, so that for greater/smaller values of σ_I/σ_Y the yield locus of AA 5182-O is interior/exterior to the von Mises ellipsoid. Note also that the results obtained for TRIP-780 steel and AA 5182-O coincide for $\sigma_I/\sigma_Y = 0$ and $\sigma_{II}/\sigma_Y = 0$, yet the yield locus of TRIP-780 steel is exterior for any other stress state.

Fig. 2 shows the evolution of the Lankford coefficient (ratio between in-plane transverse and through-thickness plastic strains under uniaxial tension) versus loading orientation for the five materials investigated in this paper. Note that for isotropic materials the Lankford coefficient is constant $r_\theta = 1$. For materials described with the Hill (1948) yield criterion, the value of r_θ is a nonlinear function of θ which shows maxima/minima for $\theta = 0°$ and $90°$. In addition, for specific combinations of the anisotropy parameters, materials modeled with Hill (1948) yield criterion show an additional maximum/minimum for an intermediate value of the loading orientation (Dasappa et al., 2012; Huh et al., 2013; Shen et al., 2019; Cazacu and Rodríguez-Martínez, 2019). Namely, for Material 1 the Lankford coefficient is greater than 1, with absolute minimum and maximum for $\theta \approx 42°$ and $90°$, respectively. For Material 2 and TRIP-780 steel the Lankford coefficient increases with the loading orientation, with r_θ smaller than 1 for $\theta < 45°$ and greater than 1 for $\theta > 45°$. Note that Material 2 is comparatively *more anisotropic* than TRIP-780 steel because the variation of the Lankford coefficient with θ is more important. For AA 5182-O the

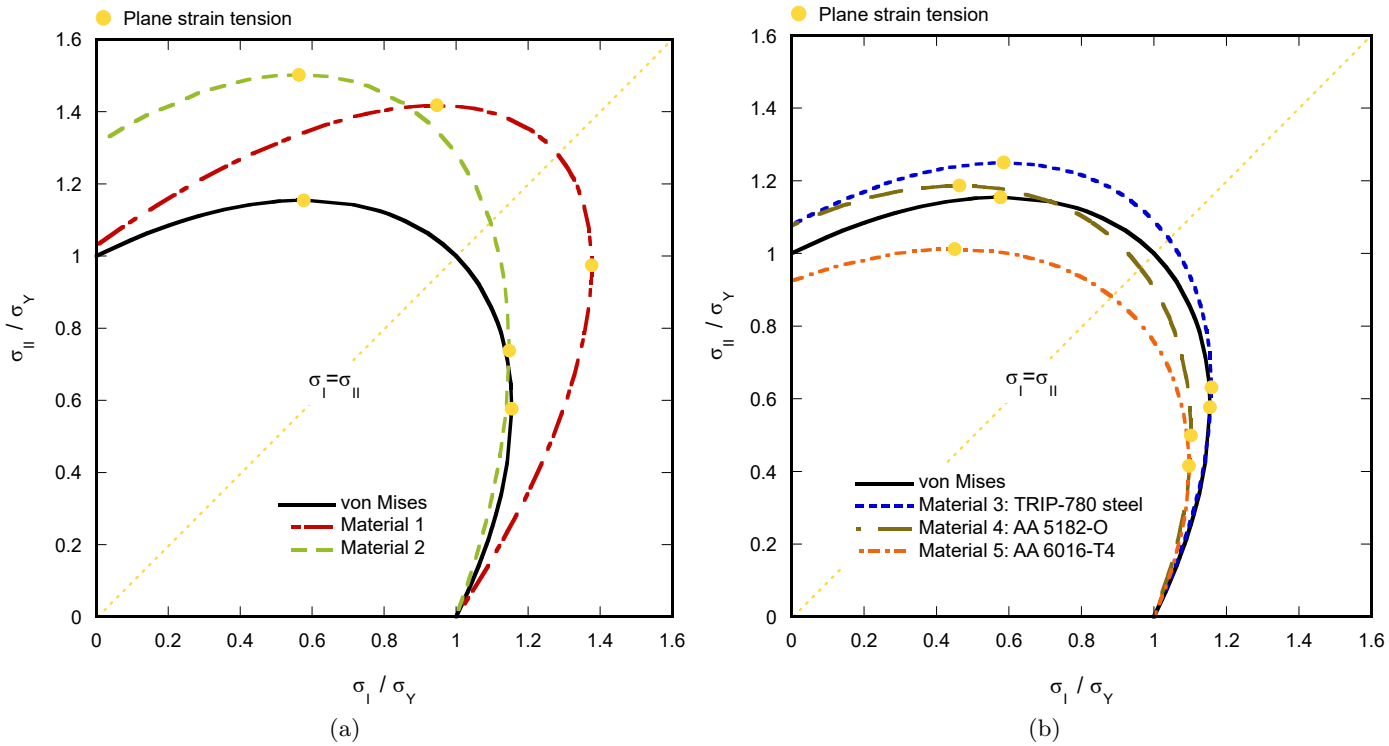

Figure 1: Normalized plane stress theoretical yield loci for biaxial loading conditions, $\sigma_{\rm II}/\sigma_Y$ versus $\sigma_{\rm I}/\sigma_Y$, according to Hill (1948) criterion. (a) Comparison between Material 1, Material 2 and von Mises material. (b) Comparison between Material 3: TRIP-780 steel, Material 4: AA 5182-O, Material 5: AA 6016-T4 and von Mises material. In Section 6 we investigate the loading cases that lie within the yellow markers that correspond to plane strain tension.

value of r_θ increases, reaches a maximum for $\theta = 50°$, and then decreases. The Lankford coefficient is slightly greater than 1 within the range $40° \leq \theta \leq 62°$, and smaller than 1 for any other loading orientation. The value of r_θ for $\theta = 90°$ is greater than for $\theta = 0°$. For AA 6016-T4 the value of r_θ is smaller than 1 for any θ, reaching the minimum for $\theta = 47°$, with the Lankford coefficient for $\theta = 0°$ being greater than for $\theta = 90°$. Sowerby and Duncan (1971) and Parmar and Mellor (1978) among others noticed that for Hill (1948) materials there is a strong coupling between the Lankford coefficient and the material formability. The general trend being that for $r_\theta > 1$ the elliptical plane stress yield locus *stretches out* (increasing the maximum curvature of the yield surface, see Material 2 in Fig. 1a) and the material formability decreases (with respect to the isotropic von Mises (1928) material), and viceversa for $r_\theta < 1$ (see Section 6).

The differences in the plane stress yield loci and the Lankford coefficient shown by the 5 materials studied will be used to explain the results presented in Section 6, and to determine the role of material orthotropy in dynamic formability.

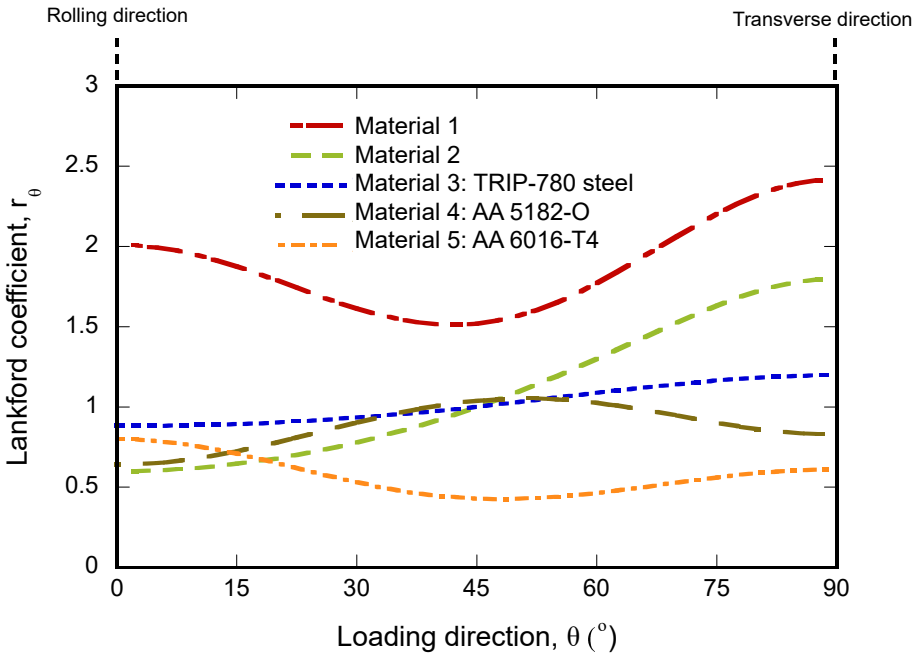

Figure 2: Lankford coefficient r_θ versus loading orientation θ. Comparison between Material 1, Material 2, Material 3: TRIP-780 steel, Material 4: AA 5182-O and Material 5: AA 6016-T4.

3. Linear stability model

The linear stability model is an extension of the 2D approach developed by Zaera et al. (2015) to orthotropic materials with yielding based on Hill (1948) criterion. We consider a thin plate of initial thickness h^0 and edges of initial length L_x^0 and L_y^0, see Fig. 3. The plate is subjected to constant and opposed stretching velocities $V_x = \pm\dot{\varepsilon}_{xx}^0 L_x^0/2$ and $V_y = \pm\dot{\varepsilon}_{yy}^0 L_y^0/2$ on opposed sides, where $\dot{\varepsilon}_{xx}^0$ and $\dot{\varepsilon}_{yy}^0$ are the imposed initial strain rates. The loading condition is determined by the ratio $\chi = \dot{\varepsilon}_{yy}^0/\dot{\varepsilon}_{xx}^0$, which is varied between 0 (plane strain stretching) and 1 (equibiaxial stretching) in the calculations presented in this paper. The Lagrangian Cartesian coordinate system associated to the applied velocity field is denoted by (X, Y, Z) while the corresponding Eulerian counterpart is denoted by (x, y, z). Note that the direction Z of the plate is assumed of plane stress. The plate displays orthotropic symmetry with the Cartesian frame of orthotropy (X_1, X_2, X_3) defined by an angle ψ between X and X_1 (see Fig. 3), with X_1, X_2 and X_3 being the rolling, transverse and through-thickness directions, respectively. Our attention is limited to the scenarios where the orthotropy axes and the loading axes are co-directional ($\psi = 0°$ or $90°$), i.e. the principal directions of stress and strain coincide. In this paper the angle ψ is also referred to as material orientation. Notice that varying the material orientation from $\psi = 0°$ to $\psi = 90°$ amounts to exchange the value of the anisotropy coefficients F and G, see equations (5) and (9). The elastic deformations are neglected and hereafter $\bar{\varepsilon} = \bar{\varepsilon}^p$ will be named effective strain and $\dot{\bar{\varepsilon}} = \dot{\bar{\varepsilon}}^p$ effective strain rate.

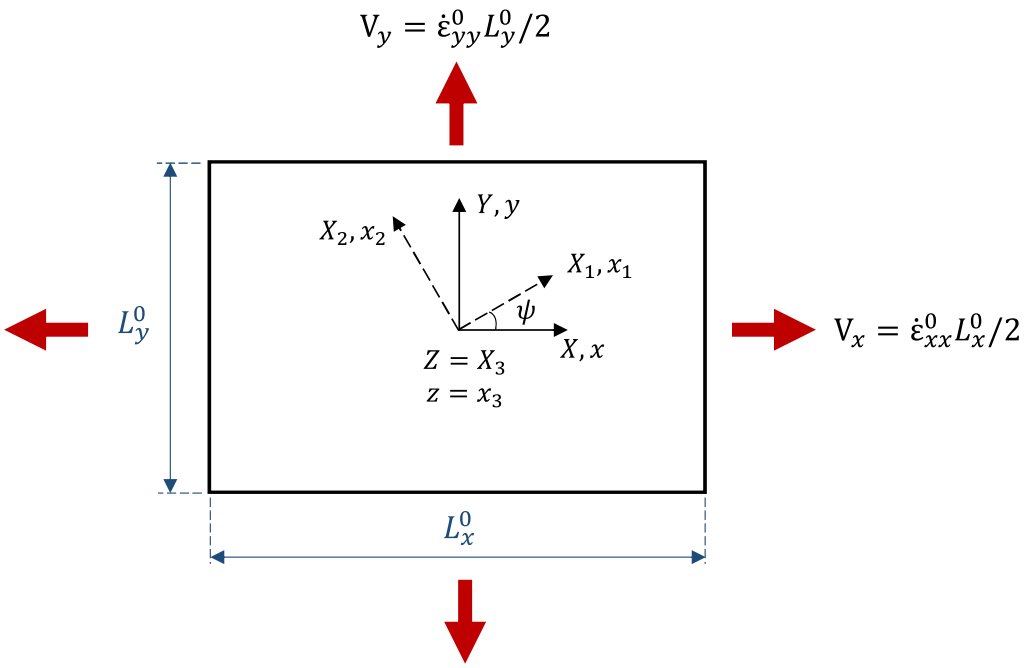

Figure 3: Linear stability analysis. Schematic representation of the geometry and boundary conditions of the problem addressed: a plate of initial thickness h^0 and edges of initial length L_x^0 and L_y^0 subjected to constant and opposed stretching velocities $V_x = \pm\dot{\varepsilon}^0_{xx} L^0_x/2$ and $V_y = \pm\dot{\varepsilon}^0_{yy} L^0_y/2$ on opposed sides, where $\dot{\varepsilon}^0_{xx}$ and $\dot{\varepsilon}^0_{yy}$ are the imposed initial strain rates. The Lagrangian Cartesian coordinate system associated to the applied velocity field is denoted by (X, Y, Z), while the corresponding Eulerian counterpart is denoted by (x, y, z). Note that the direction Z of the plate is assumed of plane stress. The plate displays orthotropic symmetry with the Cartesian frame of orthotropy (X_1, X_2, X_3) defined by an angle ψ between X and X_1.

The unknowns of the problem are: velocities (V_x, V_y), strain rates (d_{xx}, d_{yy}), deformation gradients (F_{xx}, F_{yy}, F_{zz}), thickness (h), effective strain $(\bar{\varepsilon})$, effective strain rate $(\dot{\bar{\varepsilon}})$, temperature (T), uniform stresses $(\sigma_{xx}, \sigma_{yy})$, average stress in the major stretching direction (σ_{xx}^{avg}), effective stress $(\bar{\sigma})$, yield stress in the rolling direction (σ_Y) and Bridgman's correction factor argument (φ). The fundamental equations governing the loading process are presented below:

- Kinematic relations:

$$\begin{aligned} d_{xx} &= \frac{\partial V_x}{\partial x} \\ d_{yy} &= \frac{\partial V_y}{\partial y} \end{aligned} \tag{13}$$

$$\begin{aligned} F_{xx} &= \frac{\dot{F}_{xx}}{d_{xx}} \\ F_{yy} &= \frac{\dot{F}_{yy}}{d_{yy}} \end{aligned} \tag{14}$$

- Incompressibility condition:

$$F_{xx}F_{yy}F_{zz} = 1 \tag{15}$$

- Current thickness:

$$h = h^0 F_{zz} \tag{16}$$

- Momentum balance:

$$\begin{aligned} F_{yy}\frac{\partial\left(h\sigma_{xx}^{avg}\right)}{\partial X} &= \rho h^0 \frac{\partial V_x}{\partial t} \\ F_{xx}\frac{\partial\left(h\sigma_{yy}\right)}{\partial Y} &= \rho h^0 \frac{\partial V_y}{\partial t} \end{aligned} \tag{17}$$

  where ρ is the material density (assumed constant, i.e. $\rho = \rho^0$). The momentum balance equation in the out of plane direction has been disregarded, see Zaera et al. (2015).

- Average stress in the major stretching direction:

$$\sigma_{xx}^{avg} = B\left(\varphi\right)\sigma_{xx} \tag{18}$$

  where

$$B\left(\varphi\right)=\sqrt{1+\varphi^{-1}}\ln\left(1+2\varphi+2\sqrt{\varphi\left(1+\varphi\right)}\right)-1 \tag{19}$$

is the correction factor introduced by Bridgman (1952) to model the hydrostatic stresses that developed in a necked section (see Zhou et al., 2006; Zaera et al., 2015). Notice that, while in this paper we have used the classical Bridgman (1952) approximation, in future works we shall consider the one-dimensional model based on an asymptotic analysis recently developed by Audoly and Hutchinson (2016, 2019) to determine the stress state inside the neck.

- Argument of Bridgman's correction factor:

$$\varphi=\frac{h}{8}\frac{\partial^2 h}{\partial x^2} \tag{20}$$

- Effective stress:

$$\bar{\sigma}=\left[\left(G+H\right)\sigma_{11}^2+\left(H+F\right)\sigma_{22}^2-2H\sigma_{11}\sigma_{22}+2N\sigma_{12}^2\right]^{1/2} \tag{21}$$

Previous expression is a specialization of equation (5) for plane stress conditions, where σ_{11}, σ_{22} and σ_{12} are given by:

$$\begin{aligned}\sigma_{11}&=\sigma_{xx}\cos^2\psi+\sigma_{yy}\sin^2\psi\\ \sigma_{22}&=\sigma_{xx}\sin^2\psi+\sigma_{yy}\cos^2\psi\\ \sigma_{12}&=\left(\sigma_{xx}-\sigma_{yy}\right)\sin\psi\cos\psi\end{aligned} \tag{22}$$

- Flow rule:

$$d_{xx} = \dot{\bar{\varepsilon}} \frac{\partial \bar{\sigma}}{\partial \sigma_{xx}}$$
$$d_{yy} = \dot{\bar{\varepsilon}} \frac{\partial \bar{\sigma}}{\partial \sigma_{yy}} \tag{23}$$

where

$$\dot{\bar{\varepsilon}} = \left[\frac{F d_{11}^2 + G d_{22}^2 + H(d_{11} + d_{22})^2}{FG + FH + GH} + \frac{2 d_{12}^2}{N} \right]^{1/2} \tag{24}$$

Previous expression is a particularization of equation (9) for plane stress conditions, where d_{11}, d_{22} and d_{12} are given by:

$$d_{11} = d_{xx} \cos^2 \psi + d_{yy} \sin^2 \psi$$
$$d_{22} = d_{xx} \sin^2 \psi + d_{yy} \cos^2 \psi \tag{25}$$
$$d_{12} = (d_{xx} - d_{yy}) \sin \psi \cos \psi$$

The governing equations are completed with the expressions of the yield condition, the yield stress in the rolling direction, the effective strain and the temperature evolution equation, given by the relations (4), (6), (7) and (10), respectively.

The solution of the problem at any given loading time, usually referred to as homogeneous or fundamental solution:

$$\mathbb{S}^1 = (V_x^1, V_y^1, d_{xx}^1, d_{yy}^1, F_{xx}^1, F_{yy}^1, F_{zz}^1, h^1, \dot{\bar{\varepsilon}}^1, \bar{\varepsilon}^1, T^1, \sigma_{xx}^1, \sigma_{yy}^1, \sigma_{xx}^{avg,1}, \bar{\sigma}^1, \sigma_Y^1, \varphi^1)^T \tag{26}$$

can be readily obtained by integration of the governing equations with the following initial conditions:

$$
\begin{aligned}
&V_x\left(X,Y,0\right)=\dot{\varepsilon}^0_{xx}X; \qquad V_y\left(X,Y,0\right)=\dot{\varepsilon}^0_{yy}Y; \qquad \sigma_{ij}\left(X,Y,0\right)=0\\
&\bar{\varepsilon}\left(X,Y,0\right)=0; \qquad\qquad h\left(X,Y,0\right)=h^0; \qquad\quad T\left(X,Y,0\right)=T^0=T_{ref}
\end{aligned}
\tag{27}
$$

and boundary conditions:

$$
\begin{aligned}
&V_x\left(L^0_x/2,Y,t\right)=-V_x\left(-L^0_x/2,Y,t\right)=\dot{\varepsilon}^0_{xx}L^0_x/2\\
&V_y\left(X,L^0_y/2,t\right)=-V_y\left(X,-L^0_y/2,t\right)=\dot{\varepsilon}^0_{yy}L^0_y/2
\end{aligned}
\tag{28}
$$

where, as already mentioned, $\dot{\varepsilon}^0_{xx}$ and $\dot{\varepsilon}^0_{yy}$ define the initial strain rates in X and Y directions of the plate, respectively. The applied loading is selected through input values of $\dot{\varepsilon}^0_{xx}$ and $\chi=\dot{\varepsilon}^0_{yy}/\dot{\varepsilon}^0_{xx}$. Note that $\dot{\varepsilon}^0_{xx}$ will be also referred to as imposed initial major strain rate. The details on the kinematics of the fundamental solution are given in Appendix A.

The stability of the homogeneous solution is tested by introducing at some time t^1 a small perturbation $\delta\mathbb{S}$ of the form:

$$
\delta\mathbb{S}(X,t)_{t^1}=\delta\mathbb{S}^1e^{i\xi X+\eta(t-t^1)} \tag{29}
$$

where

$$
\delta\mathbb{S}^1=\left(\delta V_x,\delta V_y,\delta d_{xx},\delta d_{yy},\delta F_{xx},\delta F_{yy},\delta F_{zz},\delta h,\delta\dot{\bar{\varepsilon}},\delta\bar{\varepsilon},\delta T,\delta\sigma_{xx},\delta\sigma_{yy},\delta\sigma^{avg}_{xx},\delta\bar{\sigma},\delta\sigma_Y,\delta\varphi\right)^T \tag{30}
$$

is the perturbation amplitude, ξ is the wavenumber (also called perturbation mode) and η is the growth rate of the perturbation at time t^1. The perturbation is imposed on lines $X=constant$ which is the orientation naturally selected by the material to trigger a neck for the loading paths ($0\leq\chi\leq1$) and the orientations of the orthotropy axes ($\psi=0^\circ$ or 90°) investigated in this work (see Zaera et al., 2015). Notice that, while in this paper we have assumed the classical frozen coefficients theory and the exponential form of the time dependency of the perturbation for the sake of simplicity, Xavier et al. (2020) have recently developed a promising method to relax these assumptions.

The perturbed solution of the problem is:

$$\mathbb{S} = \mathbb{S}^1 + \delta\mathbb{S} \tag{31}$$

with $|\delta\mathbb{S}| \ll \left|\mathbb{S}^1\right|$. A system of linear algebraic equations is obtained by substituting equation (31) into the governing equations and keeping only the first-order terms in the increments $\delta\mathbb{S}^1$. This system of equations, which is not explicitly shown in this paper for the sake of brevity, has been adimensionalized by introducing the following dimensionless groups:

$$\begin{array}{lllllll}
\hat{V}_x = \dfrac{V_x}{h^0\dot{\bar{\varepsilon}}^1}; & \hat{V}_y = \dfrac{V_y}{h^0\dot{\bar{\varepsilon}}^1}; & \hat{d}_{xx} = \dfrac{d_{xx}}{\dot{\bar{\varepsilon}}^1}; & \hat{d}_{xx} = \dfrac{d_{xx}}{\dot{\bar{\varepsilon}}^1}; & \hat{F}_{xx} = F_{xx}; & \hat{F}_{yy} = F_{yy} \\
\hat{F}_{zz} = F_{zz}; & \hat{h} = \dfrac{h}{h^0}; & \hat{\dot{\bar{\varepsilon}}} = \dfrac{\dot{\bar{\varepsilon}}}{\dot{\bar{\varepsilon}}^1}; & \hat{\bar{\varepsilon}} = \bar{\varepsilon}; & \hat{T} = \dfrac{T}{T^0}; & \hat{\sigma}_{xx} = \dfrac{\sigma_{xx}}{\sigma^0} \\
\hat{\sigma}_{yy} = \dfrac{\sigma_{yy}}{\sigma^0}; & \hat{\sigma}_{xx}^{avg} = \dfrac{\sigma_{xx}^{avg}}{\sigma^0}; & \hat{\bar{\sigma}} = \dfrac{\bar{\sigma}}{\sigma^0}; & \hat{\sigma}_Y = \dfrac{\sigma_Y}{\sigma^0}; & \hat{\varphi} = \varphi & \\
\hat{\eta} = \dfrac{\eta}{\dot{\bar{\varepsilon}}^1}; & \hat{\xi} = \xi h^0 & & & &
\end{array} \tag{32}$$

A non trivial solution for the adimensionalized perturbation amplitude $\delta\hat{\mathbb{S}}^1$ is obtained only if the determinant of the matrix of coefficients of the system of adimensionalized linear algebraic equations is equal to zero. Application of this condition leads to a third order polynomial in $\hat{\eta}$:

$$B_3(\hat{\mathbb{S}}^1)\hat{\eta}^3 + B_2(\hat{\mathbb{S}}^1, \hat{\xi})\hat{\eta}^2 + B_1(\hat{\mathbb{S}}^1, \hat{\xi})\hat{\eta} + B_0(\hat{\mathbb{S}}^1, \hat{\xi}) = 0 \tag{33}$$

with

$$
\begin{aligned}
B_3(\hat{\mathbb{S}}^1) &= 8\tilde{c}(\hat{F}^1_{xx})^3\left(\hat{M}_1(\hat{d}^1_{xx})^2 - 2\hat{R}_2\hat{d}^1_{xx}\hat{d}^1_{yy} + \hat{R}_1(\hat{d}^1_{yy})^2 + \hat{Q}_2\left(\hat{M}_1\hat{R}_1 - \hat{R}_2^2\right)\right)\\
B_2(\hat{\mathbb{S}}^1,\hat{\xi}) &= -8(\hat{F}^1_{xx})^2\left(\hat{F}^1_{xx}\left(\beta\hat{Q}_3\left(\bar{\sigma}^1\left(\hat{R}_2^2 - \hat{M}_1\hat{R}_1\right) + \hat{R}_1(\hat{d}^1_{yy})^2\right) + \right.\right.\\
&\qquad \left.\left.\tilde{c}\hat{Q}_1\left(\hat{R}_2^2 - \hat{M}_1\hat{R}_1\right) + \beta\hat{M}_1\hat{Q}_3(\hat{d}^1_{xx})^2 - 2\beta\hat{Q}_3\hat{R}_2\hat{d}^1_{xx}\hat{d}^1_{yy}\right) - \hat{\xi}^2\tilde{c}\tilde{H}^2\hat{h}^1\hat{F}^1_{yy}\left((\hat{d}^1_{yy})^2 + \hat{M}_1\hat{Q}_2\right)\right)\\
B_1(\hat{\mathbb{S}}^1,\hat{\xi}) &= \frac{2}{3}\hat{\xi}^2\tilde{H}^2\hat{h}^1\hat{F}^1_{yy}\left(-12(\hat{F}^1_{xx})^2\left(\beta\hat{Q}_3\left((\hat{d}^1_{yy})^2 - \hat{M}_1\bar{\sigma}^1\right) + \tilde{c}\left(\hat{d}^1_{xx}\left((\hat{d}^1_{yy})^2 + \hat{M}_1\hat{Q}_2\right) - \hat{M}_1\hat{Q}_1\right)\right) - \right.\\
&\qquad \left.\tilde{c}\hat{\sigma}^1_{xx}\left(12(\hat{F}^1_{xx})^2 - \hat{\xi}^2(\hat{h}^1)^2\right)\left(\hat{M}_1(\hat{d}^1_{xx})^2 - 2\hat{R}_2(\hat{d}^1_{xx})^2(\hat{d}^1_{yy})^2 + \hat{R}_1(\hat{d}^1_{yy})^2 + \hat{Q}_2\left(\hat{M}_1\hat{R}_1 - \hat{R}_2^2\right)\right)\right)\\
B_0(\hat{\mathbb{S}}^1,\hat{\xi}) &= -\frac{2}{3}\hat{\xi}^2\tilde{H}^2\hat{h}^1\hat{F}^1_{yy}\left(12\hat{d}^1_{xx}(\hat{F}^1_{xx})^2\left(\tilde{c}\hat{M}_1\hat{Q}_1 - \beta\hat{Q}_3\left((\hat{d}^1_{yy})^2 - \hat{M}_1\bar{\sigma}^1\right)\right) - \hat{\sigma}^1_{xx}\left(12(\hat{F}^1_{xx})^2 - \hat{\xi}^2(\hat{h}^1)^2\right)\right.\\
&\qquad \left.\left(\beta\hat{Q}_3\left(\bar{\sigma}^1\left(\hat{R}_2^2 - \hat{M}_1\hat{R}_1\right) + \hat{R}_1(\hat{d}^1_{yy})^2\right) + \tilde{c}\hat{Q}_1\left(\hat{R}_2^2 - \hat{M}_1\hat{R}_1\right) + \beta\hat{M}_1\hat{Q}_3(\hat{d}^1_{xx})^2 - 2\beta\hat{Q}_3\hat{R}_2\hat{d}^1_{xx}\hat{d}^1_{yy}\right)\right)
\end{aligned}
\tag{34}
$$

where $\hat{R}_1 = \sigma^0\left.\frac{\partial^2\bar{\sigma}}{\partial^2\sigma_{xx}}\right|_{t^1}$, $\hat{R}_2 = \sigma^0\left.\frac{\partial^2\bar{\sigma}}{\partial\sigma_{xx}\partial\sigma_{yy}}\right|_{t^1}$ and $\hat{M}_1 = \sigma^0\left.\frac{\partial^2\bar{\sigma}}{\partial^2\sigma_{yy}}\right|_{t^1}$ are the non-dimensional second-derivatives of the effective stress with respect to the Cauchy stress tensor components, $\hat{Q}_1 = \left.\frac{1}{\sigma^0}\frac{\partial\sigma_Y}{\partial\bar{\varepsilon}}\right|_{t_1}$, $\hat{Q}_2 = \left.\frac{\dot{\bar{\varepsilon}}^1}{\sigma^0}\frac{\partial\sigma_Y}{\partial\dot{\bar{\varepsilon}}}\right|_{t_1}$ and $\hat{Q}_3 = \left.\frac{T^1}{\sigma^0}\frac{\partial\sigma_Y}{\partial T}\right|_{t_1}$ are the non-dimensional strain, strain-rate and temperature sensitivities of the material, respectively, $\tilde{c} = \frac{\rho C_p T^0}{\sigma^0}$ is the non-dimensional specific heat, and $\frac{1}{\tilde{H}^2} = \frac{\rho\left(h^0\dot{\bar{\varepsilon}}^1\right)^2}{\sigma^0}$ represents the inertial resistance to motion.

Equation (33) has three roots in $\hat{\eta}$ which depend on the adimensionalized fundamental solution of the problem $\hat{\mathbb{S}}^1$ and the adimensionalized wavenumber $\hat{\xi}$. Note also that the adimensionalized wavenumber is related to the normalized perturbation wavelength L^0/h^0 as: $L^0/h^0 = \frac{2\pi}{\hat{\xi}}$. The requisite for unstable growth of the perturbation is given by $\Re(\hat{\eta}) > 0$. Thus, the root with the greatest positive real part denoted by $\hat{\eta}^+$ represents the physical solution of the problem (Dudzinski and Molinari, 1991). Note that $\hat{\eta}^+$ is usually referred to as instantaneous instability index (El Maï et al., 2014). Following Fressengeas and Molinari (1994), we introduce a cumulative instability index defined as $I = \int_0^t \hat{\eta}^+\dot{\bar{\varepsilon}}^1 \mathrm{d}\tau$ which tracks the history of the instantaneous grow rate of all the growing modes. To calculate I, we introduce the perturbation at different times and sum the instantaneous growth rate obtained for each loading time. The stabilizing effect of stress multiaxiality and inertia on small and large perturbation wavelengths, respectively, boosts the growth of a finite number of intermediate perturbation modes (Fressengeas and Molinari, 1994). The wavelength of the mode with the greatest value of the cumulative instability index I is called the critical cumulative wavelength, and the corresponding value of I is called the critical

cumulative instability index. The critical cumulative instability index, which evolves with the loading time, and thus with the strain, will be used in Section 6 to determine when a perturbation mode turns into a necking mode, allowing to perform quantitative comparisons between the results obtained with the linear stability analysis set out in this section, and the nonlinear two-zone model and the finite element model presented in Sections 4 and 5, respectively. Notice that Dudzinski and Molinari (1991) and Zaera et al. (2015) relied on the instantaneous instability index $\hat{\eta}^{+}$ to determine when a neck is formed, in order to construct forming limit diagrams. However, in this paper we choose I because, as discussed by El Maï et al. (2014) and Vaz-Romero et al. (2017), it provides predictions for necking formation which are generally closer to finite element results.

4. Nonlinear two-zone model

The nonlinear two-zone model is an extension to orthotropic materials with yielding based on Hill (1948) criterion of the formulation recently developed by Jacques (2020) to include inertia effects in the classical localization approach of Marciniak and Kuczyński (1967). The model consists of a plate idealized as an array of unit-cells with spatial imperfections in the form of bands with reduced initial thickness. Fig. 4 shows the schematic representation of the unit-cell. Following the notation used in Section 3, the Lagrangian and Eulerian Cartesian coordinate systems associated to the applied loading conditions are (X, Y, Z) and (x, y, z), respectively. Similarly, (X_1, X_2, X_3) is the Cartesian coordinate system associated to the orthotropy axes defined by an angle ψ between X and X_1. The initial lengths of the cell are L_x^0 and L_y^0, and the zones inside and outside the band are denoted by A and B, respectively. The initial thicknesses of zones A and B are:

$$\begin{aligned} h^{A,0} &= h^0 \left(1 - \Delta\right) \\ h^{B,0} &= h^0 \end{aligned} \tag{35}$$

where Δ is the normalized amplitude of the imperfection. Note that superscripts $()^i$ with $i = A, B$ are used to denote quantities in the zones A and B, respectively.

The initial and boundary conditions are consistent with those used in the linear stability model (see Fig. 3, and equations (27) and (28)). Note that, in the present work, the imperfection (band with reduced thickness) is assumed perpendicular to the major stretching direction X. Indeed, as earlier stated in Section 3, this is the orientation naturally selected by the material to trigger a neck for the loading paths ($0 \leq \chi \leq 1$) and material

orientations ($\psi = 0°$ or $90°$) investigated in this paper. However, this assumption can be easily relaxed to consider other material orientations. Note also that, similarly to the stability model (see Section 3), the direction Z of the cell is assumed of plane stress and elastic deformations are neglected.

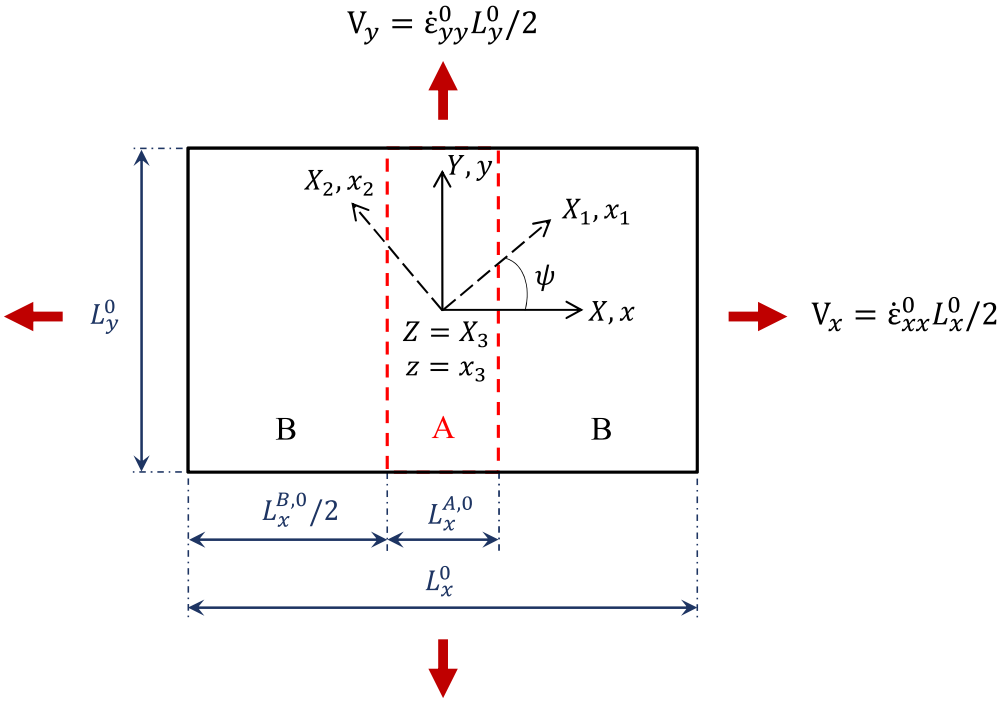

Figure 4: Two-zone model. Schematic representation of the unit-cell with two zones of uniform thickness A and B. The initial lengths of the cell are L^0_x and L^0_y, and the initial thicknesses of zones A and B are $h^{A,0}$ and $h^{B,0}$, respectively, with $h^{B,0}>h^{A,0}$. The initial and boundary conditions are consistent with those used in the linear stability model, see Fig. 3.

The zones A and B are assumed to be regions of homogeneous deformation and the unknowns of the problem in these two zones are: strain rates (d^i_{xx}, d^i_{yy}), deformation gradients ($F^i_{xx}, F^i_{yy}, F^i_{zz}$), thicknesses ($h^i$), effective strains ($\bar{\varepsilon}^i$), effective strain rates ($\dot{\bar{\varepsilon}}^i$), temperature ($T^i$), uniform stresses ($\sigma^i_{xx}, \sigma^i_{yy}$), average stress in zone A in the major stretching direction ($\sigma^{A,avg}_{xx}$), yield stresses in rolling direction (σ^i_Y) and Bridgman's correction factor argument in zone A (φ^A). The equations governing the loading process are presented below:

- Kinematic relations:

  The components of the overall deformation gradient in the whole unit-cell (F_{xx}, F_{yy}, F_{zz}) are given by equation (A.7) and the continuity of the displacement between the zones A and B leads to the following relations

linking the deformation gradient components in the zones A and B, and the overall deformation gradient components:

$$\begin{aligned} F_{xx}^{A} R + F_{xx}^{B}(1-R) &= F_{xx} \\ F_{yy}^{A} = F_{yy}^{B} &= F_{yy} \end{aligned} \tag{36}$$

where

$$R = \frac{L_x^{A,0}}{L_x^0} \tag{37}$$

is the ratio between the initial length of the imperfection, $L_x^{A,0}$, and the initial length of the cell in the major stretching direction, L_x^0.

The strain rate components in the zones A and B are given by:

$$\begin{aligned} d_{xx}^{i} &= \frac{\dot{F}_{xx}^{i}}{F_{xx}^{i}} \\ d_{yy}^{i} &= \frac{\dot{F}_{yy}^{i}}{F_{yy}^{i}} \end{aligned} \tag{38}$$

- Virtual work principle:

  Jacques (2020) stated that including inertia effects in the classical localization approach of Marciniak and Kuczyński (1967) implies that the momentum balance equation cannot be fulfilled at any point of the cell, and he circumvented this *difficulty* using the virtual principle work (i.e. the weak form of the momentum balance equation), which leads to the following differential equation to describe the evolution of F_{xx}^{A}:

$$\ddot{F}_{xx}^{A} = \frac{1}{C_d}\left(\frac{h^{B,0}\sigma_{xx}^{B}}{F_{xx}^{B}} - \frac{h^{A,0}\sigma_{xx}^{A,avg}}{F_{xx}^{A}}\right) \tag{39}$$

with

$$C_d = \frac{\rho (L_x^0)^2}{12} \left(R^2 h^{A,0} + R(1-R) h^{B,0} \right) \tag{40}$$

Note that all the unknowns of the problem can be readily computed once F_{xx}^A is obtained. The required steps to derive equation (39) are given in Jacques (2020).

Using the plane stress condition, $\sigma_{zz}^i = 0$, the Cauchy stress tensor components in zones A and B are computed as:

$$\begin{aligned} \sigma_{xx}^i &= s_{xx}^i - s_{zz}^i \\ \sigma_{yy}^i &= s_{yy}^i - s_{zz}^i \end{aligned} \tag{41}$$

where $\left(s_{xx}^i, s_{yy}^i, s_{zz}^i\right)$ are the components of the stress deviator referred to the coordinate system associated to the loading axes. Moreover, with respect to the orthotropy axes, they can be computed as:

$$\begin{aligned} s_{11}^i &= \frac{\sigma_Y^i}{\dot{\bar{\varepsilon}}^i} \frac{F}{(FH+FG+HG)} d_{11}^i \\ s_{22}^i &= \frac{\sigma_Y^i}{\dot{\bar{\varepsilon}}^i} \frac{F}{(FH+FG+HG)} d_{22}^i \\ s_{33}^i &= \frac{\sigma_Y^i}{\dot{\bar{\varepsilon}}^i} \frac{F}{(FH+FG+HG)} d_{33}^i \\ s_{12}^i &= \frac{\sigma_Y^i}{\dot{\bar{\varepsilon}}^i} \frac{d_{12}^i}{N} \end{aligned} \tag{42}$$

where the relationship between $\left(s_{xx}^i, s_{yy}^i, s_{zz}^i\right)$ and $\left(s_{11}^i, s_{22}^i, s_{33}^i, s_{12}^i\right)$ is calculated using the corresponding rotation matrix, as in equation (22). These expressions have been obtained using equations (8) and (21). Note that the expression of the shear component s_{12}^i is given for completeness but, for the material orientations considered in the present study ($\psi = 0°$ and $\psi = 90°$), s_{12}^i is equal to zero.

The governing equations are completed with the expressions of the yield stress in the rolling direction, the

effective strain, the temperature evolution equation, the incompressibility condition, the current thicknesses, the average stress in the major stretching direction in zone A and the effective strain rate. These expressions are given by equations (6), (7), (10), (15), (16), (18) and (24), respectively. Note that the argument of the Bridgman correction factor is calculated using the following expression (see Jacques (2020) for more details):

$$\varphi^A = \frac{\pi^2 h^A \left(h^B - h^A\right)}{16(L_x^{A,0} F_{xx}^A)^2} \tag{43}$$

The equations governing the loading process have been integrated using the explicit Euler method. In the calculations we consider that $L_x^0 = L_y^0 = L^0$. The results of the model are obtained for several normalized cell sizes $0.25 \leq L^0/h^0 \leq 10$ and h^0 fixed ($h^0 = 2$ mm). The normalized cell size in the two-zone model is the counterpart of the normalized perturbation wavelength in the linear stability analysis, see Section 3, and thus it will be denoted the same L^0/h^0. The normalized amplitude of the imperfection is $\Delta = 0.2\%$ in most two-zone calculations presented in this work (unless otherwise noted). This value is arbitrary and we take it because the same imperfection amplitude was used in the finite element calculations performed by N'souglo et al. (2020). The specific influence of the imperfection amplitude in the two-zone model results is investigated in Section 6.5. Moreover, the two-zone model results are dependent on the value of R (see equation (37)). In the case of isotropic materials, Jacques (2020) found that the value $R = 0.28$ gives the best agreement between the finite element simulations and the dynamic two-zone model, and therefore the same value is used in the present study. It will be seen in Section 6 that this value also yields an excellent agreement between the two-zone model and the finite element computations for the different anisotropic materials and within the whole range of loading conditions considered.

5. Finite element model

The finite element model is based on the unit-cell model developed by Xue et al. (2008), and later adopted by Rodríguez-Martínez et al. (2017) and N'souglo et al. (2020), to study the influence of constitutive behavior and inertia on neck formation in thin metal plates subjected to dynamic loading. The model consists of a plate modeled as an array of unit-cells with sinusoidal spatial imperfections defined by the following expression:

$$h = \frac{h^0}{2} - \frac{\delta}{2}\left[1 + \cos\left(\frac{2\pi X}{L_x^0}\right)\right] \tag{44}$$

where δ is the amplitude of the imperfection. Due to the symmetry of the model, only one eight of the cell has been analyzed (see Fig. 5), with reference configuration (imperfection-free) given by the domain $0 \leq X \leq L_x^0/2$, $0 \leq Y \leq L_y^0/2$ and $0 \leq Z \leq h^0/2$, with $L_x^0 = L_y^0 = L^0$. The origin of coordinates of the Lagrangian Cartesian coordinate system (X, Y, Z) is located at the center of mass of the whole cell. Similarly to the dynamic two-zone model (see Section 4), we have investigated several normalized cell sizes $0.25 \leq L^0/h^0 \leq 10$ with h^0 fixed ($h^0 = 2$ mm). As in the two-zone model, the normalized imperfection amplitude is $\Delta = \frac{2\delta}{h^0} = 0.2\%$ in most of the finite element calculations (unless otherwise noted). Nevertheless, the role of Δ in the finite element results is discussed in Section 6.5. The finite element calculations are performed with ABAQUS/Explicit (2016) under the following imposed initial conditions:

$$\begin{aligned} V_x\left(X,Y,Z,0\right) &= \dot{\varepsilon}_{xx}^0 X \\ V_y\left(X,Y,Z,0\right) &= \dot{\varepsilon}_{yy}^0 Y \\ V_z\left(X,Y,Z,0\right) &= -\left(\dot{\varepsilon}_{xx}^0 + \dot{\varepsilon}_{yy}^0\right) Z \\ T\left(X,Y,Z,0\right) &= T^0 = T_{ref} \end{aligned} \tag{45}$$

and boundary conditions:

$$\begin{aligned} &U_x\left(0,Y,Z,t\right) = 0; \qquad U_y\left(X,0,Z,t\right) = 0; \qquad U_z\left(X,Y,0,t\right) = 0 \\ &V_x\left(L_x^0/2,Y,Z,t\right) = \dot{\varepsilon}_{xx}^0 L_x^0/2; \qquad V_y\left(X,L_y^0/2,Z,t\right) = \dot{\varepsilon}_{yy}^0 L_y^0/2 \end{aligned} \tag{46}$$

consistent with those used in the theoretical approaches (see Sections 3 and 4) and the symmetry imposed to the finite element model (note that U_x, U_y and U_z denote displacements along the X, Y and Z directions, respectively). As shown by Rodríguez-Martínez et al. (2017), these initial conditions allow to minimize the propagation of stress waves within the unit-cell during the loading process. Similarly to the theoretical models (see Sections 3 and 4), the finite element calculations have been carried out for loading paths ranging between plane strain stretching and equibiaxial stretching ($0 \leq \chi \leq 1$), namely, we have performed calculations for $\chi = 0$, 0.125, 0.25, 0.375, 0.5, 0.625, 0.75 and 1. Each marker in Figs. 7, 8, 9, 10, 12, 13, 14 and C.16 corresponds to a value of χ. Notice that unit-cell calculations with *ab initio* geometric imperfections do not allow for exploring loading paths such that $\chi < 0$. The problem is that the orientation that has to be assigned to the imperfection such that it is aligned with the direction of zero stretch when necking occurs is not known in advance (see Hill (1952)). Moreover, the major stretching

direction of the cell, which coincides with the X axis (see Fig. 5), has been aligned either with the rolling direction ($\psi = 0°$ in the theoretical models) or the transverse direction ($\psi = 90°$ in the theoretical models).

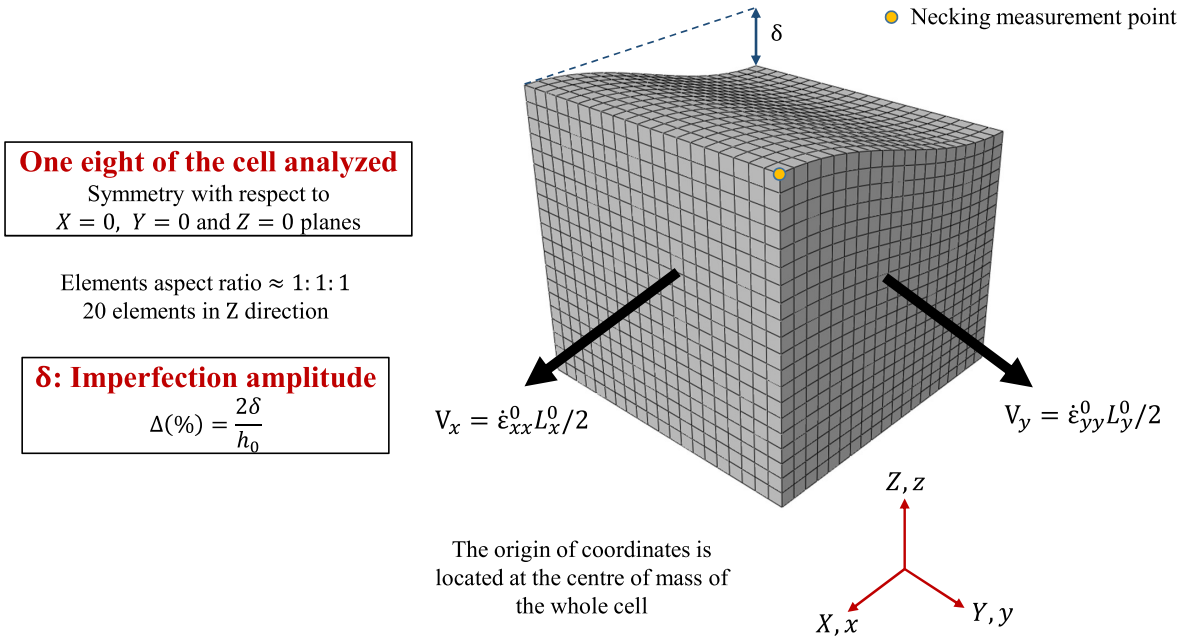

Figure 5: Finite element model. Mesh and boundary conditions for a normalized cell size of $L^0/h^0 = 1$. A large imperfection amplitude has been shown in the figure for better illustration of the geometric perturbation. For interpretation of the references to color in the text, the reader is referred to the web version of this article.

The cell is meshed with eight-node solid elements, with reduced integration and hourglass control (C3D8R in ABAQUS notation). The elements have an initial aspect ratio close to 1:1:1 with dimensions $\approx 50 \times 50 \times 50$ μm^3. The number of elements is ranging between 500 for $L^0/h^0 = 0.25$ and 800000 for $L^0/h^0 = 10$. A mesh convergence study has been performed, in which the time evolution of different output variables, namely stress, strain and necking inception, were compared for different mesh sizes. The regularizing effects of inertia and strain-rate sensitivity minimize the mesh sensitivity of the numerical calculations (see Needleman, 1988; Jacques et al., 2012; Czarnota et al., 2017; Rodríguez-Martínez et al., 2017).

The constitutive model presented in Section 2 has been implemented in ABAQUS/Explicit (2016) through a user subroutine VUMAT, adapting the implicit integration algorithm developed by Zaera and Fernández-Sáez (2006) for von Mises plasticity to Hill (1948) yield criterion.

6. Analysis and results

This section presents quantitative comparisons between the results obtained with the three approaches set out in Sections 3, 4 and 5. Section 6.1 shows the process that we have followed to determine the strain leading to necking formation and the specific methodology that we have designed to construct the forming limit diagrams, and Sections 6.2, 6.3, 6.4 and 6.5 investigate the effects of anisotropy, loading rate, strain-rate sensitivity, adiabatic heating and imperfection amplitude in the formability of the materials investigated. The finite element simulations are considered as the reference approach to validate the capacity of the stability analysis and the two-zone model to predict dynamic formability of metallic ductile materials.

6.1. Salient features

The results shown in this section correspond to Material 1 for $m = 0$ (rate-independent material) and $\beta = 0$ (isothermal conditions of deformation). The imposed initial major strain rate is $\dot{\varepsilon}^0_{xx} = 10000\ \text{s}^{-1}$. This value lies within the typical strain rates attained in electrohydraulic and electromagnetic forming operations (Golovashchenko et al., 2013; Alves Zapata, 2016). For the two-zone model and the finite element calculations the normalized imperfection amplitude is $\Delta = 0.2\%$.

Fig. 6 shows the major necking strain ε^{neck}_{xx} versus L^0/h^0. In the linear stability analysis, the major necking strain corresponds to the major logarithmic strain of the fundamental solution, $\varepsilon_{xx} = \ln(F_{xx})$, when the cumulative instability index meets the condition $I = I^{neck}$ with $I^{neck} = 3.25$. This specific value has been obtained following the calibration procedure developed by N'souglo et al. (2020) which is detailed in Appendix B (additional stability analysis results obtained using an alternative calibration procedure are included in Appendix C for completeness). In the two-zone model the major necking strain corresponds to the major logarithmic strain measured in zone B, $\varepsilon^B_{xx} = \ln\left(F^B_{xx}\right)$, when the condition $\dfrac{\dot{F}^B_{xx}}{\dot{F}^A_{xx}} = 10^{-2}$ is met (the same criterion was applied in Jacques (2020)). Similarly, in the finite element calculations, the major necking strain corresponds to the major logarithmic strain measured in the finite element located at the upper right corner of the thickest section of the cell (see the yellow marker in Figure 5) when the axial strain rate equals $10^{-3}\ \text{s}^{-1}$ in that specific element (similar procedure was applied in Rodríguez-Martínez et al. (2017) and N'souglo et al. (2020)).

First, let us note that the shape of the $\varepsilon^{neck}_{xx} - L^0/h^0$ curves obtained with the three approaches is the same. The major necking strain first decreases, reaches a minimum and then increases. The greater values of ε^{neck}_{xx} obtained for small and large values of L^0/h^0 are due to the stabilizing effects of stress multiaxiality and inertia on short and long necking wavelengths, respectively (Fressengeas and Molinari, 1994). The minimum value of the major

necking strain is referred to as the critical major necking strain ε_{xx}^c, and the corresponding value of L^0/h^0 is called the critical necking wavelength $\left(L^0/h^0\right)^c$. Figs. 6a and 6b show the results for $\chi = 0$ (plane strain stretching) and $\psi = 0°$ and $\psi = 90°$, respectively. The predictions obtained from the stability analysis and the two-zone model show excellent quantitative agreement with the finite element calculations for the whole range of values of L^0/h^0 investigated. To be noted that the stability analysis was calibrated for an isotropic von Mises material, plane strain stretching and the same strain rate, see Appendix B. Figs. 6c and 6d show the results for greater value of the loading path $\chi = 0.5$, and the same material orientations, $\psi = 0°$ and $\psi = 90°$. The predictions of the stability analysis and the two-zone model are again in good agreement with the finite element calculations, yet it is worse than in the case of $\chi = 0$. The two-zone model overestimates/underestimates the major necking strains for short/long values of L^0/h^0, however it provides accurate predictions for the critical major necking strains. Moreover, the stability analysis predictions increasingly underestimate the finite element results as L^0/h^0 increases, being the predictions for the critical major necking strains $\approx 10\%$ lower.

The critical major necking strains ε_{xx}^c, and the corresponding critical minor necking strains ε_{yy}^c (i.e. the minor logarithmic strains, at the same measurement location, when ε_{xx}^c are measured), are combined to construct the forming limit diagrams shown in Fig. 7. The results correspond to loading cases ranging from plane strain stretching $\varepsilon_{yy}^c = 0$ (i.e. $\chi = 0$) to $\varepsilon_{xx}^c = \varepsilon_{yy}^c$ (which corresponds to $\chi = 1$ for the linear stability analysis, and to $\chi < 1$ for the two-zone model and the finite element simulations, because of the strain gradients caused by the geometric imperfection, see Appendix D). In fact, the result corresponding to $\chi = 1$ for the finite element calculations is not shown in Fig. 7 since ε_{yy}^c becomes greater than ε_{xx}^c (notice that there are only seven markers corresponding to the finite element results). The cases for the material orientations $\psi = 0°$ and $90°$ are compared with the corresponding specialization to isotropic von Mises (1928) plasticity obtained by imposing $F = G = H = 0.5$ and $L = M = N = 1.5$ (see Section 2). There is a monotonic increase of ε_{xx}^c as the value of χ increases, i.e. plane strain corresponds to a minimum in the critical major necking strain. This trend is consistent with experimental, numerical and analytical results published elsewhere (Kuroda and Tvergaard, 2000; Banabic et al., 2010; Brunet and Morestin, 2001). Moreover, note that the three approaches show that the critical major necking strains ε_{xx}^c are greater for the von Mises specialization than for $\psi = 0°$ and $\psi = 90°$, with increasing differences as the condition $\varepsilon_{xx}^c = \varepsilon_{yy}^c$ is approached. Sowerby and Duncan (1971) showed that for Hill (1948) materials the influence of anisotropy on the formability is small near plane strain and increases as the loading path approaches equibiaxial tension. Moreover, note that the gap between the results obtained for $\psi = 0°$ and $\psi = 90°$ is small, with the

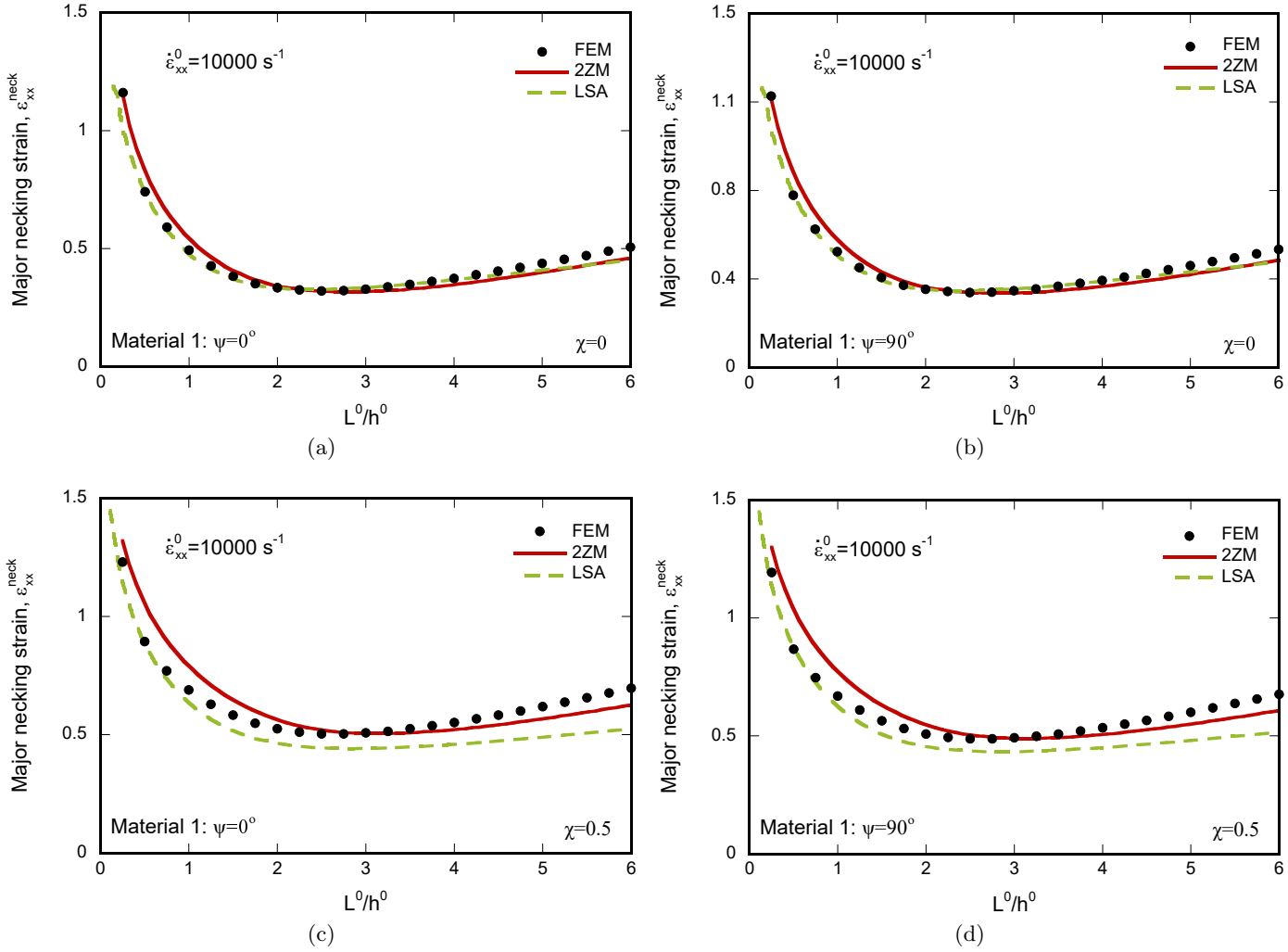

Figure 6: Comparison between finite element results (FEM), two-zone model (2ZM) and linear stability analysis predictions (LSA) for Material 1 with $m = 0$ (rate-independent) and $\beta = 0$ (isothermal conditions of deformation). Major necking strain ε_{xx}^{neck} versus L^0/h^0. Different loading paths and material orientations are considered: (a) $\chi = 0$ and $\psi = 0°$, (b) $\chi = 0$ and $\psi = 90°$, (c) $\chi = 0.5$ and $\psi = 0°$ and (d) $\chi = 0.5$ and $\psi = 90°$. The imposed initial major strain rate is $\dot{\varepsilon}_{xx}^{0} = 10000$ s^{-1}. For the finite element calculations and the two-zone model the normalized imperfection amplitude is $\Delta = 0.2\%$. In the linear stability analysis the cumulative instability index is $I^{neck} = 3.25$.

lowest formability corresponding to the latter material orientation. Attending to the results presented in Fig. 2, it seems that a Lankford coefficient greater than 1 implies a drop in formability compared to the von Mises material, and the greater the value of r_θ, the greater the formability decrease (see also Sowerby and Duncan (1971) and Parmar and Mellor (1978)). Namely, the fact that r_θ is greater for $\theta = 90°$ than for $0°$ makes that the values of ε^c_{xx} are smaller for $\psi = 90°$ than for $\psi = 0°$. Moreover, it is remarkable the ability of both analytical approaches to capture the slight effect of material orientation in the forming limit diagram predicted by the finite element calculations. In addition, the results of the two-zone model show excellent quantitative agreement with the numerical computations, for all the loading paths, both material orientations and the von Mises specialization. In contrast, the stability analysis predictions, while showing very good agreement with the finite elements near plane strain, increasingly underestimate the numerical results as the condition $\varepsilon^c_{xx} = \varepsilon^c_{yy}$ is approached. There are two probable reasons behind this difference. First, the hypothesis of $I^{neck} = constant$ is a rather crude assumption that should be reassessed in a future work with the aim of finding the functional dependence of the critical instability conditions with the loading path (note that performing the calibration of the linear stability analysis for a loading case different from plane strain strechting does not to lead to a better agreement with the finite element results, see Appendix C). Second, while in the stability analysis the strain field is assumed homogeneous until the condition $I^{neck} = 3.25$ is met, in the two-zone model and the finite element calculations it is not. The imperfection leads to strain gradients along the principal loading direction such that the actual ratio between minor and major strain when the necking condition is met is greater than that corresponding to the fundamental (homogeneous) solution for $\chi > 0$, see Appendix D for details.

6.2. The effect of anisotropy

The results shown in this section correspond to Material 2, ..., Material 5 with $m = 0$ (rate-independent materials) and $\beta = 0$ (isothermal conditions of deformation). As in Section 6.1, $\dot{\varepsilon}^0_{xx} = 10000\ s^{-1}$, $\Delta = 0.2\%$ and $I^{neck} = 3.25$.

Fig. 8 compares forming limit diagrams obtained with the finite element calculations, the two-zone model and the linear stability analysis, for loading cases ranging from plane strain stretching $\varepsilon^c_{yy} = 0$ (i.e. $\chi = 0$) to $\varepsilon^c_{xx} = \varepsilon^c_{yy}$. The results correspond to (a) Material 2, (b) Material 3: TRIP-780 steel, (c) Material 4: AA 5182-O and (d) Material 5: AA 6016-T4. The cases for the material orientations $\psi = 0°$ and $90°$ are compared with the corresponding specialization to isotropic von Mises plasticity. As mentioned in Section 6.1, the influence of anisotropy increases as the loading path moves away from plane strain, in agreement with the results of Sowerby

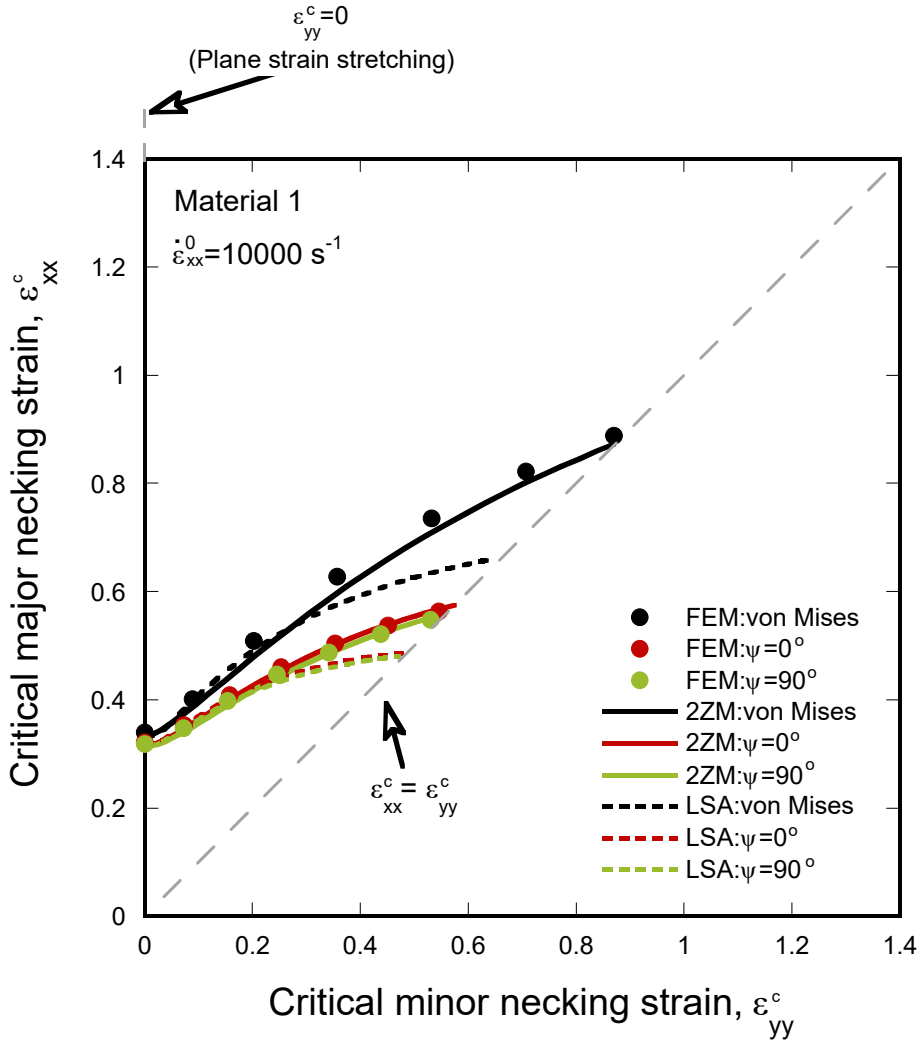

Figure 7: Comparison between finite element results (FEM), two-zone model (2ZM) and linear stability analysis predictions (LSA) for Material 1 with $m = 0$ (rate-independent) and $\beta = 0$ (isothermal conditions of deformation). Forming limit diagram, critical major necking strain ε^c_{xx} versus critical minor necking strain ε^c_{yy}, for loading conditions ranging from $\varepsilon^c_{yy} = 0$ ($\chi = 0$, plane strain stretching) to $\varepsilon^c_{xx} = \varepsilon^c_{yy}$. The cases for the material orientations $\psi = 0^\circ$ and $\psi = 90^\circ$, are compared with the corresponding isotropic von Mises material for which $F = G = H = 0.5$ and $L = M = N = 1.5$. The imposed initial major strain rate is $\dot{\varepsilon}^0_{xx} = 10000\ \mathrm{s}^{-1}$. For the finite element calculations and the two-zone model the normalized imperfection amplitude is $\Delta = 0.2\%$. In the linear stability analysis the cumulative instability index is $I^{neck} = 3.25$.

and Duncan (1971) and Kuroda and Tvergaard (2000). This overall trend is also captured by both two-zone model and stability analysis.

Similarly to the formability results presented in previous section for Material 1, the two-zone model provides predictions which are closer than the stability analysis to the finite element results, notably for large values of χ. On the other hand, for the four materials, both stability analysis and two-zone model predict the specific order of the curves obtained for the two values of ψ and for the specialization to the isotropic von Mises material. Namely, for Material 2 and Material 3 (TRIP-780 steel), Figs. 8a and 8b, the greatest formability is achieved for $\psi = 0°$, and the lowest for $\psi = 90°$, with the intermediate values of ε_{xx}^c corresponding to the von Mises specialization. These results are consistent with Sowerby and Duncan (1971) and Parmar and Mellor (1978) and the interpretation provided in Section 6.1 on the influence of the Lankford coefficient in the formability: the fact that r_θ is minimum and smaller than 1 for $\theta = 0°$ leads to the greatest critical major necking strains for $\psi = 0°$, and the fact that r_θ is maximum and greater than 1 for $\theta = 90°$ leads to the lowest critical major necking strains for $\psi = 90°$ (see Fig. 2). Comparing the finite element results for these two materials, it is observed that the influence of anisotropy in the formability results is particularly important for Material 2, and this trend is also captured by both two-zone model and linear stability analysis. These results are also consistent with the fact that the increase of the Lankford coefficient from $\theta = 0°$ to $90°$ is more important for Material 2 than for Material 3 (see Fig. 2). On the other hand, for Material 4 (AA 5182-O), Fig. 8c, the influence of material anisotropy on the formability is different than for Material 2 and Material 3, so that now the lowest formability corresponds to the von Mises specialization (contrary to Material 1 for which the largest formability was for the von Mises specialization, see Fig. 7). This also can be interpreted in terms of r_θ which, for AA 5182-O, is lower than 1 for both $\theta = 0°$ and $90°$, leading to values of ε_{xx}^c for both material orientations, $\psi = 0°$ and $90°$, which are greater than for the von Mises specialization (see Fig. 2). For Material 5 (AA 6016-T4), Fig. 8d, the lowest fomability corresponds to the von Mises specialization, as in the case of Material 4 (AA 5182-O). However, the greatest values of ε_{xx}^c are obtained for $\psi = 90°$. These results are explained because the Lankford coefficient is smaller than 1, which implies that the formability for both $\psi = 0°$ and $90°$ is greater than for the von Mises specialization. In addition, since the smallest value of r_θ is obtained for $\theta = 90°$, the greatest values of the critical major necking strain are obtained for the material orientation $\psi = 90°$ (see Fig. 2).

Even if our results show a clear correlation between formability and the value of the Lankford coefficient in the main straining direction, it is worth emphasizing that, strictly speaking, the forming limit diagram of an anisotropic material depends on the whole yield locus. For instance, it can be noticed that, for Material 1, the

forming limit curves for the two orientations are very close while the Lankford coefficient in the transverse direction is significantly larger than in the rolling direction ($r_\theta\,(0°) = 2.01$ and $r_\theta\,(90°) = 2.42$), see Figs. 2 and 7. The weak influence of orientation on the formability of Material 1 is probably related to the fact that its yield surface is nearly symmetrical with respect to the $\sigma_{\rm I} = \sigma_{\rm II}$ line (Fig. 1a). Also, we have to mention that the strong influence of the Lankford coefficient on formability is specific to the Hill 48 yield function. Indeed, several studies (dedicated to quasi-static conditions) have shown that with non-quadratic yield criteria the influence of the Lankford coefficient is much less pronounced (Parmar and Mellor, 1978; Graf and Hosford, 1990; Friedman and Pan, 2000).

6.3. The effect of loading rate

The results presented in this section correspond to Material 1, ..., Material 5, with $m = 0$ (rate-independent materials) and $\beta = 0$ (isothermal conditions of deformation), for imposed initial major strain rates $\dot{\varepsilon}^0_{xx}$ ranging from 500 s^{-1} to 50000 s^{-1}. While the largest strain rates exceed the maximum values typically attained in high energy rate forming processes, which are approximately 20000 s^{-1} (see the Introduction of this paper), exploring such a wide range of loading rates helps to enlighten the role of inertia in the formability of anisotropic materials. As in Sections 6.1 and 6.2, $\Delta = 0.2\%$ and $I^{neck} = 3.25$.

Fig. 9 shows forming limit diagrams obtained with the finite element calculations, and the two theoretical models, for loading cases ranging from plane strain stretching $\varepsilon^c_{yy} = 0$ (i.e. $\chi = 0$) to $\varepsilon^c_{xx} = \varepsilon^c_{yy}$. The results are obtained for (a) Material 1, (b) Material 2, (c) Material 3: TRIP-780 steel, (d) Material 4: AA 5182-O and (e) Material 5: AA 6016-T4. The cases for the material orientations $\psi = 0°$ and $90°$ are compared with the corresponding specialization to isotropic von Mises plasticity. The difference with Figs. 7 and 8 is that the imposed initial major strain rate has been reduced by half $\dot{\varepsilon}^0_{xx} = 5000$ s^{-1}. The two-zone model results and the stability analysis predictions show qualitative agreement with the finite element calculations for the five materials considered, capturing the relative order of the $\varepsilon^c_{xx} - \varepsilon^c_{yy}$ curves obtained for the two values of ψ and for the specialization to von Mises plasticity (the relative order of the curves is the same as in the case of $\dot{\varepsilon}^0_{xx} = 10000$ s^{-1}). The quantitative agreement between two-zone model and finite elements is excellent, for all the loading paths. On the other hand, the predictions of the stability analysis gradually deviate from the finite element results as χ increases. As mentioned in Section 6.1, this difference is partially attributed to the fact in the two-zone model and the finite element calculations the imperfection leads to strain gradients along the principal loading direction, such that the ratio between minor and major strain when the necking condition is met is greater than the theoretical one corresponding to the stability analysis (decreasing the imperfection amplitude improves the agreement between

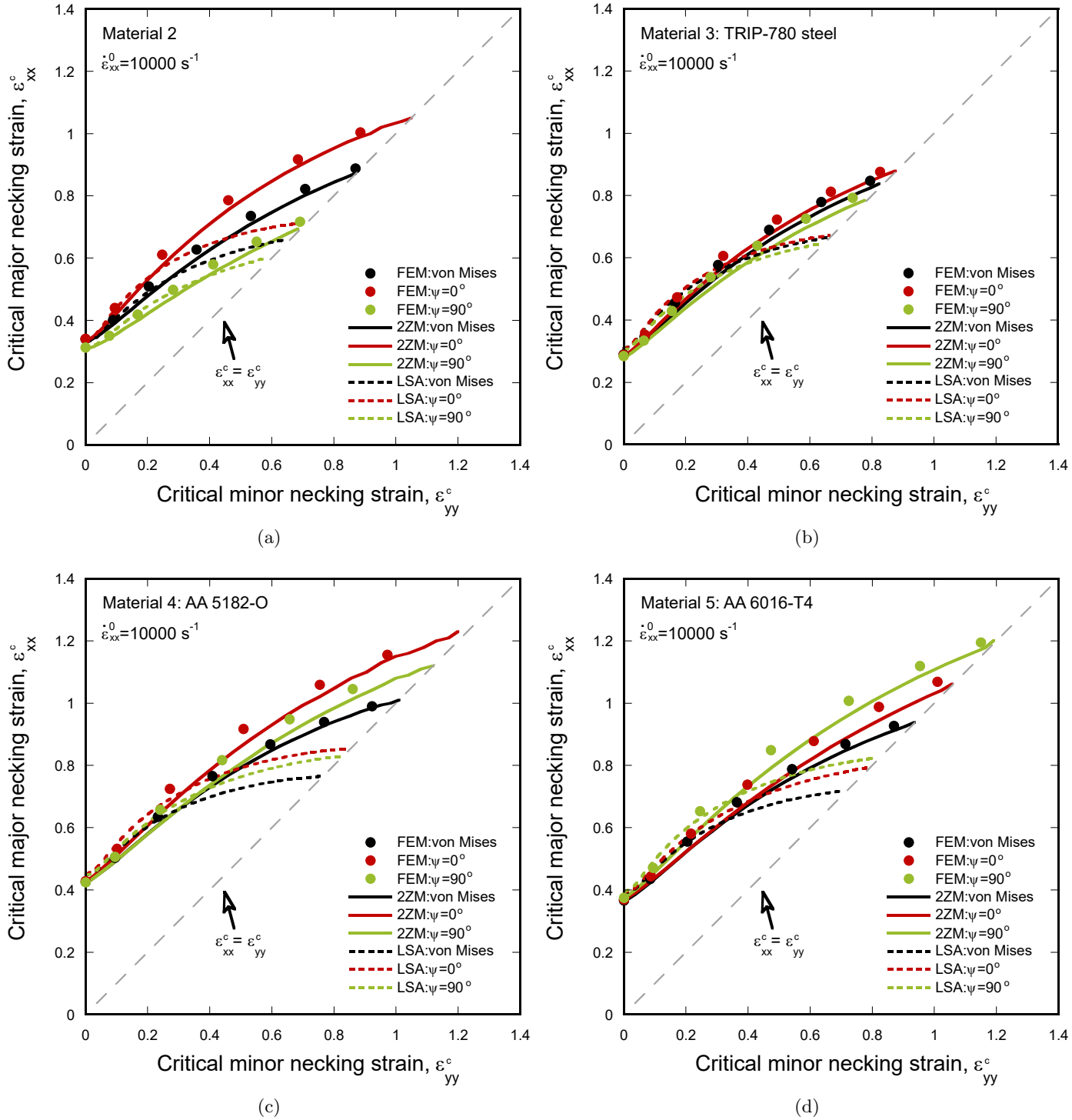

Figure 8: Comparison between finite element results (FEM), two-zone model (2ZM) and linear stability analysis predictions (LSA). Forming limit diagram, critical major necking strain ε^c_{xx} versus critical minor necking strain ε^c_{yy}, for loading conditions ranging from $\varepsilon^c_{yy} = 0$ ($\chi = 0$, plane strain stretching) to $\varepsilon^c_{xx} = \varepsilon^c_{yy}$. The results correspond to (a) Material 2, (b) Material 3: TRIP-780 steel, (c) Material 4: AA 5182-O, (d) Material 5: AA 6016-T4. The strain-rate sensitivity parameter is $m = 0$ (rate-independent materials) and the Taylor-Quinney coefficient is $\beta = 0$ (isothermal conditions of deformation). The cases for the material orientations $\psi = 0^\circ$ and $\psi = 90^\circ$, are compared with the corresponding isotropic von Mises material for which $F = G = H = 0.5$ and $L = M = N = 1.5$. The imposed initial major strain rate is $\dot{\varepsilon}^0_{xx} = 10000$ s^{-1}. For the finite element calculations and the two-zone model the normalized imperfection amplitude is $\Delta = 0.2\%$. In the linear stability analysis the cumulative instability index is $I^{neck} = 3.25$.

linear stability analysis, two-zone model and finite elements, see Section 6.5). The hypothesis of $I^{neck} = constant$ also seems to play a role in this disagreement.

Fig. 10 shows the same results as in Fig. 9 for an imposed initial major strain rate which is four times greater $\dot{\varepsilon}^0_{xx} = 20000\ \mathrm{s}^{-1}$. Notice that for the five materials considered, the relative order of the $\varepsilon^c_{xx} - \varepsilon^c_{yy}$ curves for $\psi = 0°$, $\psi = 90°$ and the von Mises specialization, is the same obtained for lower strain rates in Figs. 7, 8 and 9. In other words, the finite element calculations show that the strain rate does not change the relative influence of the plastic anisotropy on the dynamic formability of the materials investigated, and such behaviour is captured by the stability analysis and the two-zone model.

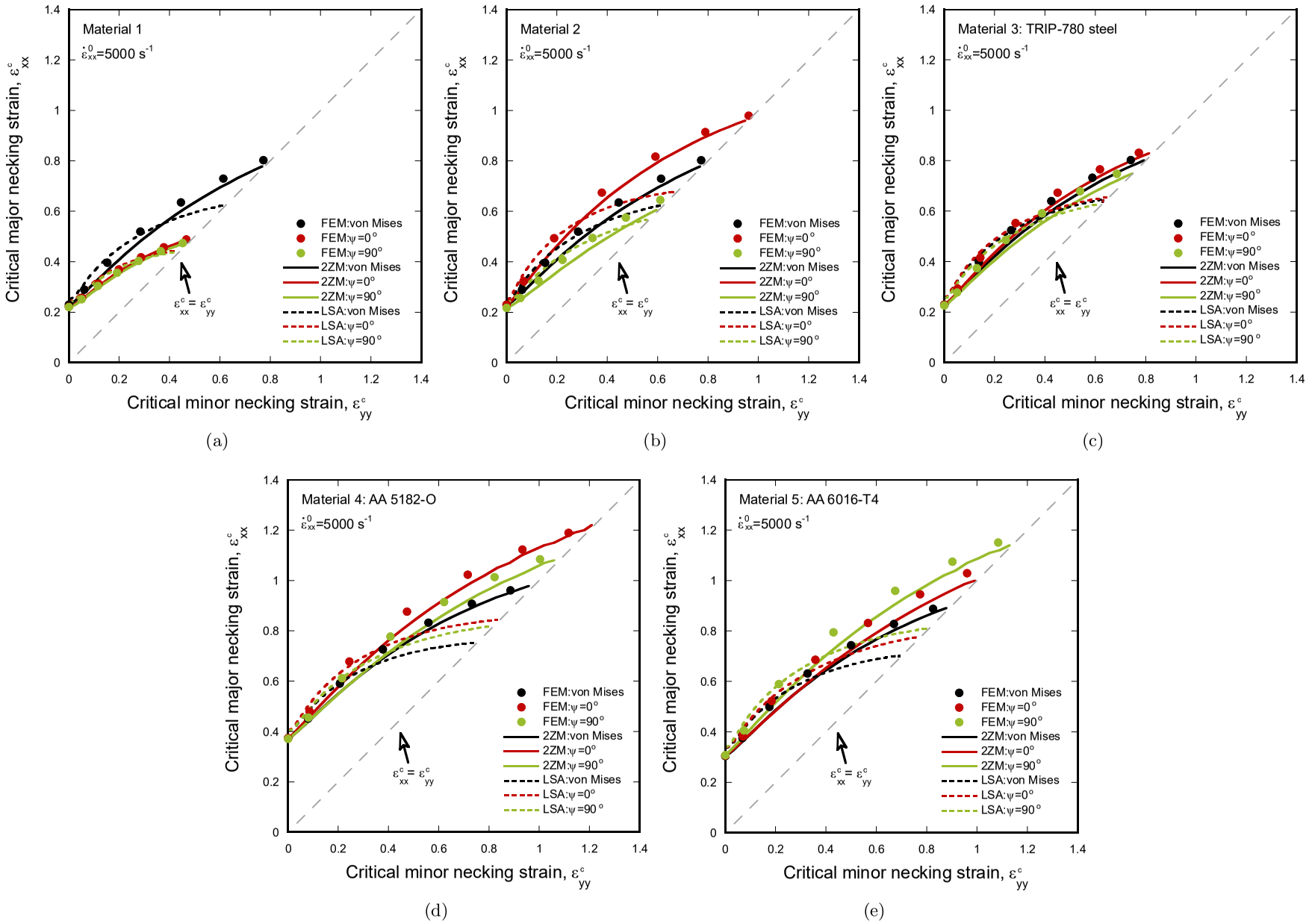

Figure 9: Comparison between finite element results (FEM), two-zone model (2ZM) and linear stability analysis predictions (LSA). Forming limit diagram, critical major necking strain ε^c_{xx} versus critical minor necking strain ε^c_{yy}, for loading conditions ranging from $\varepsilon^c_{yy} = 0$ ($\chi = 0$, plane strain stretching) to $\varepsilon^c_{xx} = \varepsilon^c_{yy}$. The results correspond to (a) Material 1, (b) Material 2, (c) Material 3: TRIP-780 steel, (d) Material 4: AA 5182-O and (e) Material 5: AA 6016-T4. The strain-rate sensitivity parameter is $m = 0$ (rate-independent materials) and the Taylor-Quinney coefficient is $\beta = 0$ (isothermal conditions of deformation). The cases for the material orientations $\psi = 0^\circ$ and $\psi = 90^\circ$, are compared with the corresponding isotropic von Mises material for which $F = G = H = 0.5$ and $L = M = N = 1.5$. The imposed initial major strain rate is $\dot{\varepsilon}^0_{xx} = 5000$ s^{-1}. For the finite element calculations and the two-zone model the normalized imperfection amplitude is $\Delta = 0.2\%$. In the linear stability analysis the cumulative instability index is $I^{neck} = 3.25$.

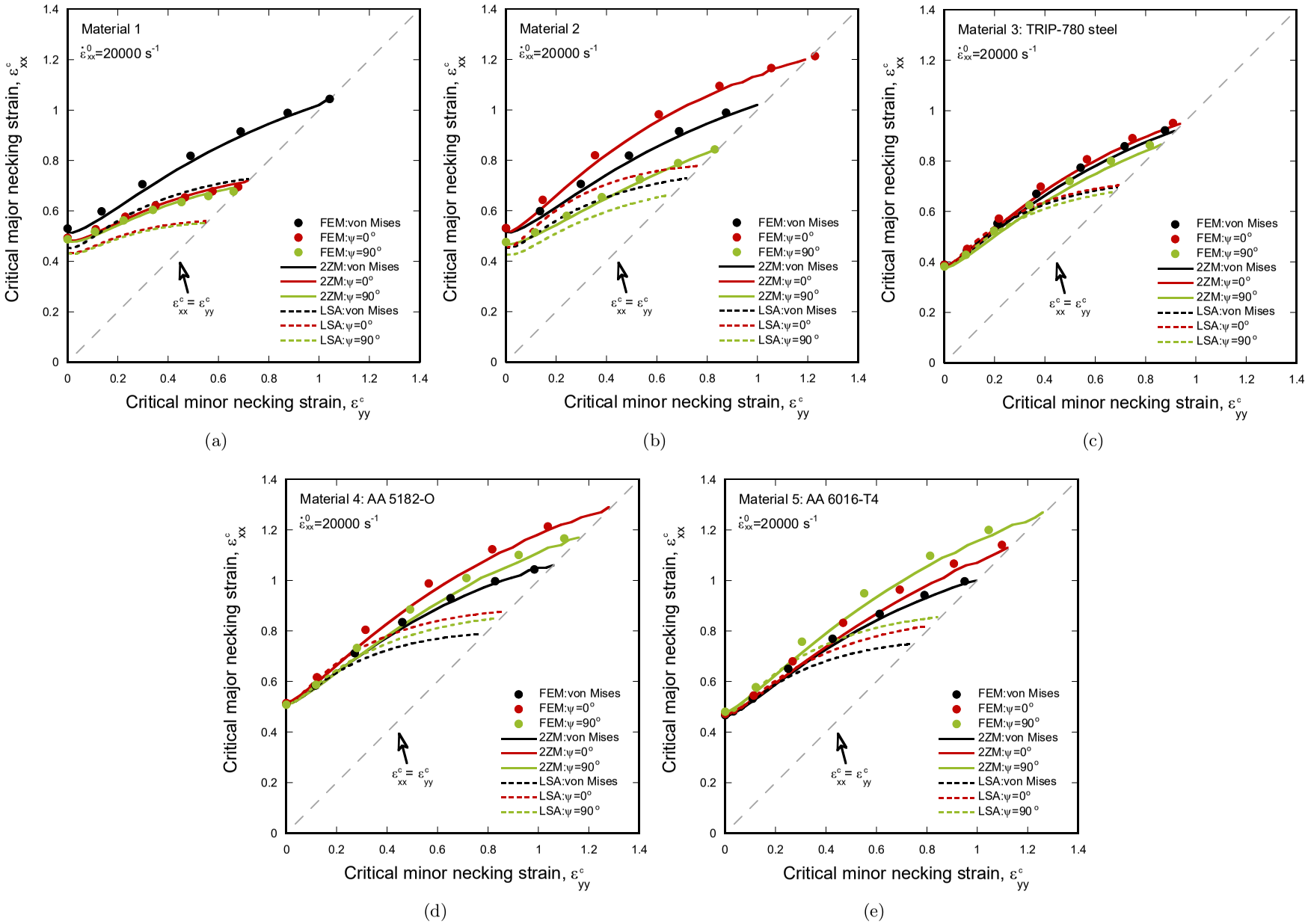

Figure 10: Comparison between finite element results (FEM), two-zone model (2ZM) and linear stability analysis predictions (LSA). Forming limit diagram, critical major necking strain ε^c_{xx} versus critical minor necking strain ε^c_{yy}, for loading conditions ranging from $\varepsilon^c_{yy} = 0$ ($\chi = 0$, plane strain stretching) to $\varepsilon^c_{xx} = \varepsilon^c_{yy}$. The results correspond to (a) Material 1, (b) Material 2, (c) Material 3: TRIP-780 steel, (d) Material 4: AA 5182-O and (e) Material 5: AA 6016-T4. The strain-rate sensitivity parameter is $m = 0$ (rate-independent materials) and the Taylor-Quinney coefficient is $\beta = 0$ (isothermal conditions of deformation). The cases for the material orientations $\psi = 0°$ and $\psi = 90°$, are compared with the corresponding isotropic von Mises material for which $F = G = H = 0.5$ and $L = M = N = 1.5$. The imposed initial major strain rate is $\dot{\varepsilon}^0_{xx} = 20000$ s^{-1}. For the finite element calculations and the two-zone model the normalized imperfection amplitude is $\Delta = 0.2\%$. In the linear stability analysis the cumulative instability index is $I^{neck} = 3.25$.

The stabilizing effect of strain rate is brought out in Fig. 11, which shows the evolution of the critical major necking strain ε^c_{xx} with the imposed initial major strain rate $\dot{\varepsilon}^0_{xx}$, for the five materials considered and $\chi = 0$ (plane strain stretching). As in previous plots, results are presented for $\psi = 0^\circ$, $\psi = 90^\circ$ and the specialization to von Mises material. The critical major necking strain increases nonlinearly with the axial strain rate displaying a concave-upwards shape. Namely, the slope of the $\varepsilon^c_{xx} - \dot{\varepsilon}^0_{xx}$ curves is very shallow until ≈ 2000 s^{-1} (the precise value depends on the material), when it starts to increase rapidly with the strain rate. This transition in the slope of the $\varepsilon^c_{xx} - \dot{\varepsilon}^0_{xx}$ curves determines when inertia effects become important, leading to neck retardation and increasing material formability (Jacques, 2020). Recall that inertia effects are size dependent and, if the specimen is thinner/thicker, inertia effects become important for greater/smaller strain rates (see Fig. 11 in Jacques (2020)). The predictions of the two-zone model find excellent agreement with the finite elements for all the strain rates investigated, while the stability analysis underestimates the finite element results and the two-zone model calculations for the greater strain rates considered. This disagreement is most likely due to the simple criterion used in the stability analysis, which assumes that necking occurs for the same value of cumulative index $I^{neck} = 3.25$ for all the strain rates. Moreover, the increase of the critical major necking strain ε^c_{xx} with the strain rate is largely independent of the anisotropy (as anticipated by the comparison of Figs. 7, 8, 9 and 10), as evidenced by the fact that for the five materials considered the $\varepsilon^c_{xx} - \dot{\varepsilon}^0_{xx}$ curves for $\psi = 0^\circ$, $\psi = 90^\circ$ and the von Mises specialization, are virtually parallel to each other. However, the effect of inertia on the necking strain does depend on the material considered. For instance, for the material orientation $\psi = 0^\circ$, the two-zone model predicts that the increase of the critical major necking strain from 100 s^{-1} to 20000 s^{-1} (maximum strain rate typically attained in high energy rate forming processes, see the Introduction of this paper), calculated as $\Delta\varepsilon^c_{xx}|^{20000\ \mathrm{s}^{-1}}_{100\ \mathrm{s}^{-1}} = \dfrac{\varepsilon^c_{xx}|_{20000\ \mathrm{s}^{-1}} - \varepsilon^c_{xx}|_{100\ \mathrm{s}^{-1}}}{\varepsilon^c_{xx}|_{100\ \mathrm{s}^{-1}}}$, is 436%, 490%, 166%, 77% and 120% for Materials $1, ..., 5$, respectively. Notice that, for aluminium alloys (Materials 4 and 5), with lower density than steel, inertia effects are less important, and the increase of necking strain with the strain rate is smaller. On the other hand, the lower influence of inertia on Material 3, in comparison with Materials 1 and 2, is most likely due to the greater yield stress of TRIP-780 steel, which decreases inertial resistance to motion (see equation (34)). Moreover, we have checked that the same overall trends and conclusions are obtained for loading paths other than plane strain, however, we do not show additional plots for the sake of brevity. On the other hand, it is worth mentioning that, as shown in the works of Rodríguez-Martínez et al. (2017) and Jacques (2020), the increase of the loading parameter decreases the influence of inertia on neck formation. For instance, for $\psi = 0^\circ$ and greater loading parameter $\chi = 0.5$, the two-zone model predicts that the increase of the critical major necking

strain $\Delta\varepsilon^c_{xx}|^{20000\ \mathrm{s}^{-1}}_{100\ \mathrm{s}^{-1}}$ is 95%, 45%, 22%, 10% and 17% for Materials $1, ..., 5$, respectively. Notice that for the five materials the value of $\Delta\varepsilon^c_{xx}|^{20000\ \mathrm{s}^{-1}}_{100\ \mathrm{s}^{-1}}$ is smaller than in the case of plane strain. For additional discussions on the interplay between inertia and loading path, the reader is referred to Section 9 of Rodríguez-Martínez et al. (2017) and Section 3.2 of Jacques (2020).

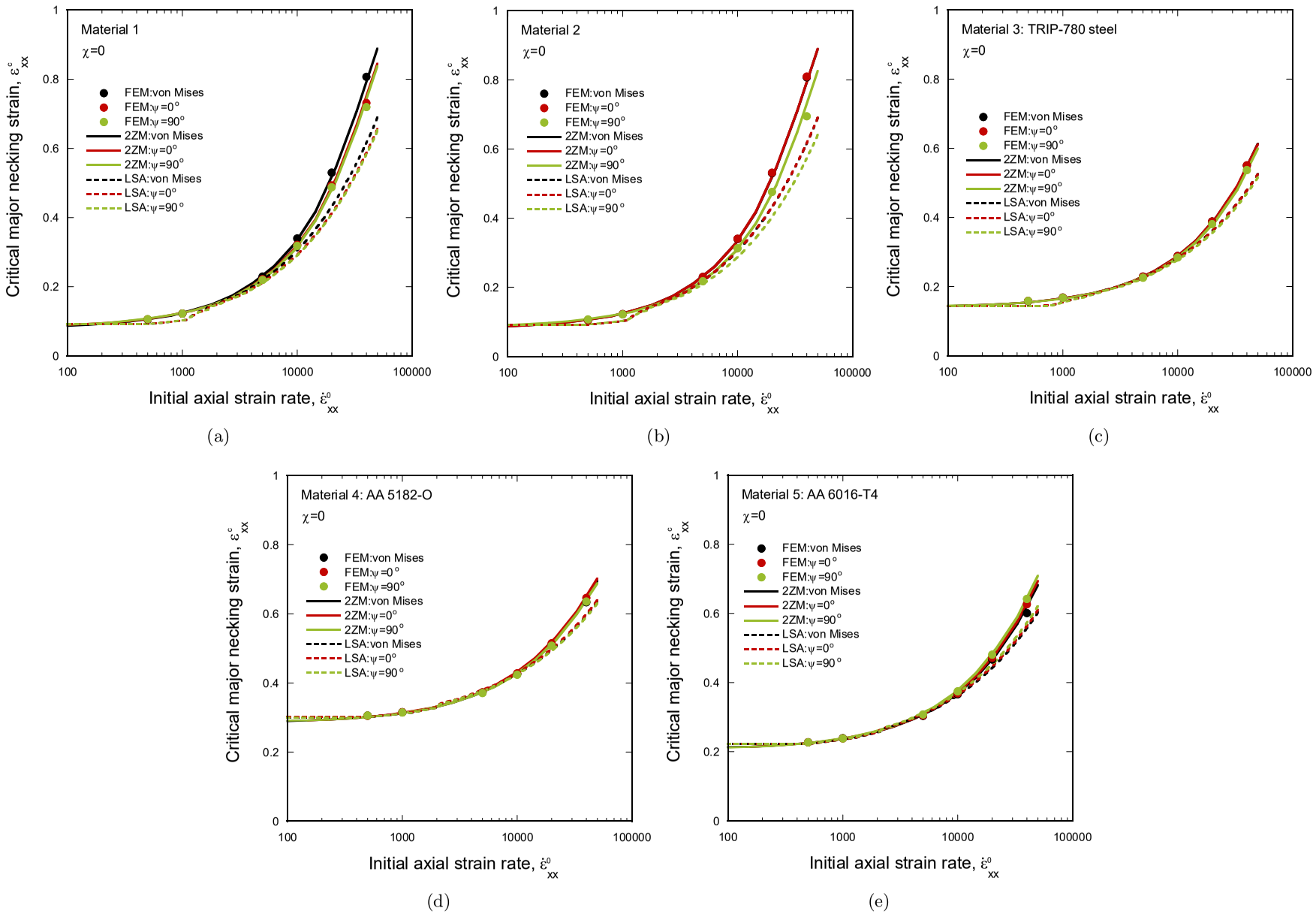

Figure 11: Comparison between finite element results (FEM), nonlinear two-zone model (2ZM) and linear stability analysis predictions (LSA). Critical necking strain ε^c_{xx} versus imposed initial major strain rate $\dot{\varepsilon}^0_{xx}$. The loading path is $\chi = 0$ (plane strain stretching). The results correspond to (a) Material 2, (b) Material 3: TRIP-780 steel, (c) Material 4: AA 5182-O, (d) Material 5: AA 6016-T4. The strain-rate sensitivity parameter is $m = 0$ (rate-independent materials) and the Taylor-Quinney coefficient is $\beta = 0$ (isothermal conditions of deformation). The cases in which the major loading direction coincides with the rolling and transverse directions, $\psi = 0^\circ$ and $\psi = 90^\circ$, are compared with the isotropic von Mises material for which $F = G = H = 0.5$ and $L = M = N = 1.5$. For the finite element calculations and the two-zone model the normalized imperfection amplitude is $\Delta = 0.2\%$. In the linear stability analysis the cumulative instability index is $I^{neck} = 3.25$.

6.4. The effect of strain-rate sensitivity and adiabatic heating

The results shown in this section correspond to Material 1, with two different values of the strain-rate sensitivity exponent $m = 0.01$ and 0.02, for isothermal ($\beta = 0$) and adiabatic conditions of deformation ($\beta = 0.9$). Similar values of the strain-rate sensitivity exponent have been reported in the literature for different metals and alloys (e.g. see Hutchinson and Neale (1977)). The Taylor-Quinney coefficient $\beta = 0.9$ is a standard value generally taken for metals and alloys (e.g. Børvik et al. (2001); Dey et al. (2004); Park et al. (2018)). As in Sections 6.1 and 6.2, $\dot{\varepsilon}^0_{xx} = 10000$ s^{-1}, $\Delta = 0.2\%$ and $I^{neck} = 3.25$.

Fig. 12 shows forming limit diagrams obtained with the three approaches developed in this paper. The cases for the material orientations $\psi = 0°$ and 90° are compared with the corresponding specialization to isotropic von Mises plasticity. The results correspond to (a) $m = 0.01$ and (b) $m = 0.02$. The Taylor-Quinney coefficient is $\beta = 0$ (isothermal conditions of deformation). The increase of the strain-rate sensitivity parameter delays necking formation, shifting upwards the $\varepsilon^c_{xx} - \varepsilon^c_{yy}$ curves and increasing material formability. For instance, for $\chi = 0$ and $\psi = 0°$, the two-zone model predicts that the value of ε^c_{xx} increases from ≈ 0.32 for the rate-independent material (see Fig. 7) to ≈ 0.39 for $m = 0.02$. Note that the effect of strain-rate hardening on neck retardation has been previously shown in the literature, e.g. see Hutchinson and Neale (1977) and Audoly and Hutchinson (2019). On the other hand, notice that the increase of the critical major necking strain with the strain-rate sensitivity exponent $\Delta\varepsilon^c_{xx}|^{m=0.02}_{m=0}$ predicted by the two-zone model, which is 21% for plane strain, is significantly smaller than the gain in ε^c_{xx} obtained when the imposed initial major strain rate is increased from 100 s^{-1} to 20000 s^{-1}, which is 436% (see Fig. 11a). This result shows that at high strain rates, the inertia effect is most likely the main contributor to neck retardation (under quasi-static loading, when a power law relation is adopted, equation (6), the increase in ductility due strain-rate sensitivity is independent of the prescribed strain-rate, see Hutchinson and Neale (1977)). Moreover, for the results presented in this section, the increase of the critical major necking strain with the material viscosity shows a mild variation with the loading path, since for material orientation $\psi = 0°$ and $\varepsilon^c_{xx} = \varepsilon^c_{yy}$, we have that $\Delta\varepsilon^c_{xx}|^{m=0.02}_{m=0} = 11\%$, being this value slightly smaller than for plane strain. On the other hand, notice that the value of the strain-rate sensitivity parameter does not amend the effect of material anisotropy in the forming limit diagram. In fact, the goal of presenting the results for different values of m in different plots (instead of showing in each plot results for a given material orientation and different values of m) is to illustrate that the effect of anisotropy in the formability remains virtually the same for different material viscosities. As in the case of the rate-independent material (see Fig. 7), for $m = 0.01$ and 0.02 the critical major necking strains are significantly greater for the von Mises specialization than for $\psi = 0°$ and $\psi = 90°$, with increasing differences as

the loading path moves away from plane strain. Notice also that for both values of m considered, the formability of the material is slightly greater for $\psi = 0°$ than for $\psi = 90°$.

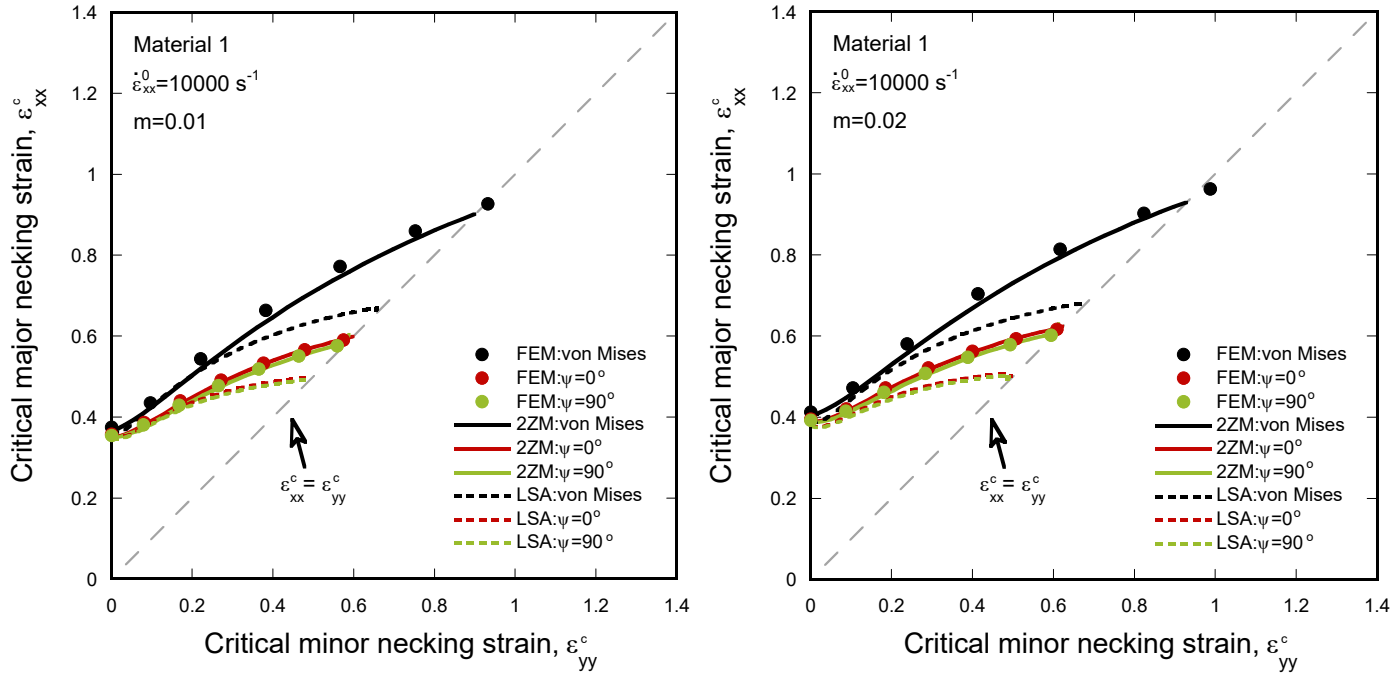

(a) (b)

Figure 12: Comparison between finite element results (FEM), nonlinear two-zone model (2ZM) and linear stability analysis predictions (LSA). Forming limit diagram, critical major necking strain ε^c_{xx} versus critical minor necking strain ε^c_{yy}, for loading conditions ranging from $\varepsilon^c_{yy} = 0$ ($\chi = 0$, plane strain stretching) to $\varepsilon^c_{xx} = \varepsilon^c_{yy}$. The results correspond to Material 1 with two different values of the strain-rate sensitivity parameter: (a) $m = 0.01$ and (b) $m = 0.02$. The cases for the material orientations $\psi = 0°$ and $\psi = 90°$, are compared with the corresponding isotropic von Mises material for which $F = G = H = 0.5$ and $L = M = N = 1.5$. The imposed initial major strain rate is $\dot{\varepsilon}^0_{xx} = 10000$ s^{-1}. The Taylor-Quinney coefficient is $\beta = 0$ (isothermal conditions of deformation). For the finite element calculations and the two-zone model the normalized imperfection amplitude is $\Delta = 0.2\%$. In the linear stability analysis the cumulative instability index is $I^{neck} = 3.25$.

Fig. 13 compares forming limit diagrams obtained with the three approaches developed in this paper, for isothermal ($\beta = 0$) and adiabatic ($\beta = 0.9$) conditions of deformation. The strain-rate sensitivity exponent is $m = 0.01$. The results correspond to (a) specialization to isotropic von Mises plasticity, (b) material orientation $\psi = 0°$ and (c) material orientation $\psi = 90°$. Notice that the scales of Figs. 13a and 13b-13c are different. Thermal softening favors necking formation, decreasing material formability. The three approaches predict the same trend, with the $\varepsilon^c_{xx} - \varepsilon^c_{yy}$ curves shifting downwards between 2% and 8% for $\beta = 0.9$, within the range of loading paths considered. Moreover, these results indicate that thermal softening does not change the specific influence of anisotropy on the material formability, suggesting that the conclusions derived in this work using $\beta = 0$ (see Sections 6.1, 6.2, 6.3 and 6.5) remain valid for adiabatic conditions of deformation.

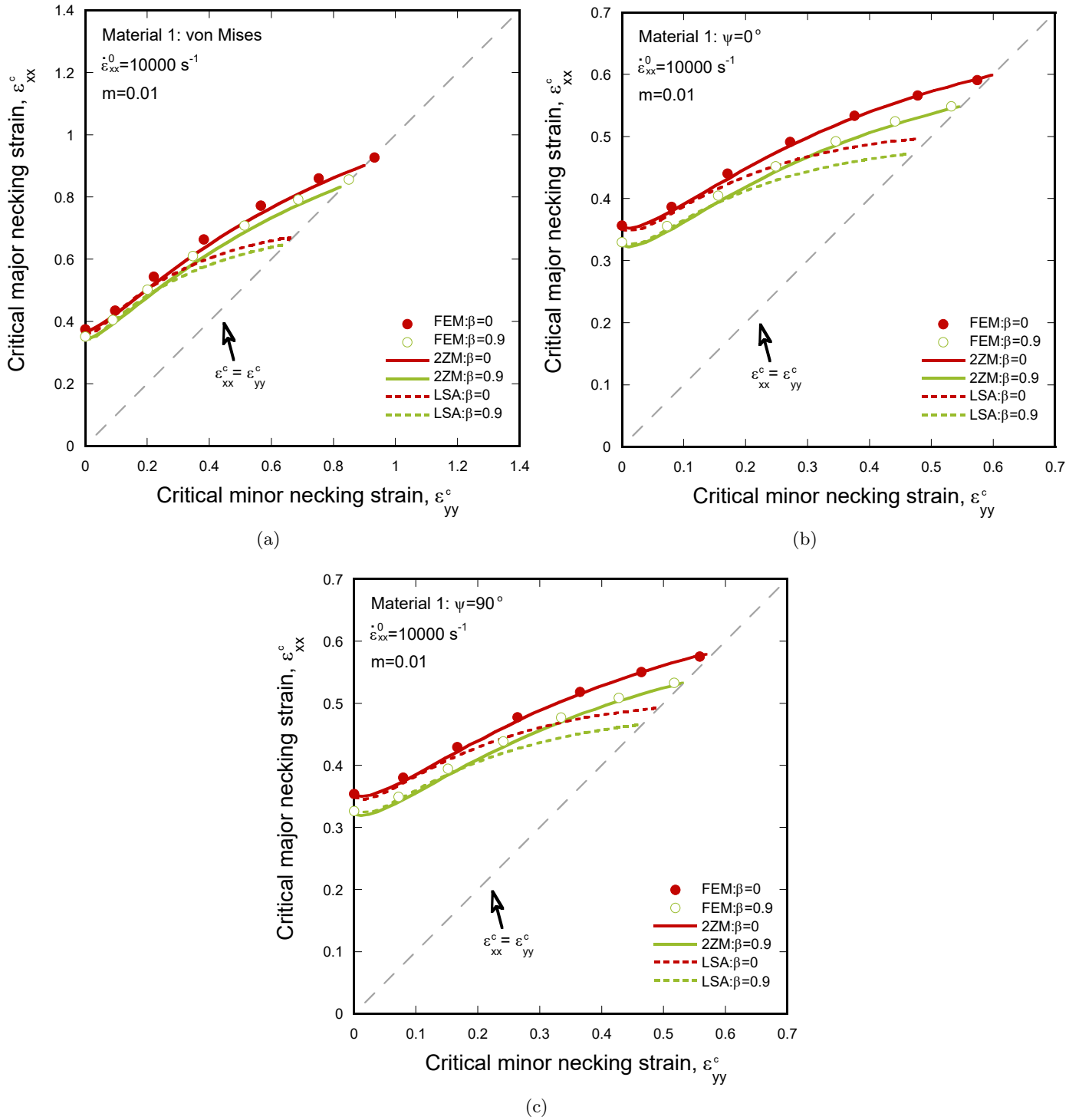

Figure 13: Comparison between finite element results (FEM), nonlinear two-zone model (2ZM) and linear stability analysis predictions (LSA). Forming limit diagram, critical major necking strain ε^c_{xx} versus critical minor necking strain ε^c_{yy}, for loading conditions ranging from $\varepsilon^c_{yy} = 0$ ($\chi = 0$, plane strain stretching) to $\varepsilon^c_{xx} = \varepsilon^c_{yy}$. The results correspond to Material 1 for: (a) specialization to von Mises plasticity for which $F = G = H = 0.5$ and $L = M = N = 1.5$, (b) material orientation $\psi = 0°$ and (c) material orientation $\psi = 90°$. The strain-rate sensitivity parameter is $m = 0.01$. The imposed initial major strain rate is $\dot{\varepsilon}^0_{xx} = 10000\ \text{s}^{-1}$. Results are shown for isothermal ($\beta = 0$) and adiabatic ($\beta = 0.9$) conditions of deformation. For the finite element calculations and the two-zone model the normalized imperfection amplitude is $\Delta = 0.2\%$. In the linear stability analysis the cumulative instability index is $I^{neck} = 3.25$.

6.5. The effect of imperfection amplitude

The results shown in this section correspond to Material 1 with $m = 0$ (rate-independent material) and $\beta = 0$ (isothermal conditions of deformation). The finite element calculations and the two-zone model have been performed with two different values of the imperfection amplitude $\Delta = 0.02\%$ and 2%, i.e. ten times smaller and ten times greater than the imperfection amplitude used in the rest of the calculations of this paper. The value of the cumulative index has been calibrated for these two additional imperfection amplitudes such that I^{neck} is 5.55 and 1.12, respectively, see Appendix B. Note that, as Δ increases, the cumulative instability index I^{neck} decreases (see also Fig. 10 of Zheng et al. (2020) and the discussion therein, and Appendix C of N'souglo et al. (2020)). As in Sections 6.1, 6.2 and 6.4, the imposed initial major strain rate is $\dot{\varepsilon}^0_{xx} = 10000\ \mathrm{s}^{-1}$.

Fig. 14 displays forming limit diagrams, ε^c_{xx} versus ε^c_{yy}, obtained with the unit-cell finite element calculations, and the two theoretical approaches developed in this paper. The results for $\psi = 0°$ and 90° are compared with the corresponding specialization to isotropic von Mises plasticity. The calculations correspond to (a) $\Delta = 0.02\%$ and (b) $\Delta = 2\%$. The critical major necking strain decreases as the imperfection amplitude increases and the cumulative instability index decreases (notice that the scales of Figs. 14a and 14b are different). Obviously, increasing the imperfection amplitude leads to early necking formation (e.g. see Hutchinson and Neale (1977), Hutchinson et al. (1978a), Rodríguez-Martínez et al. (2017) and Jacques (2020)). Namely, the two-zone model predicts that for the material orientation $\psi = 0°$, the variation in the critical major necking strain is $\Delta\varepsilon^c_{xx}|^{2\%}_{0.02\%} = \dfrac{\varepsilon^c_{xx}|_{2\%} - \varepsilon^c_{xx}|_{0.02\%}}{\varepsilon^c_{xx}|_{0.02\%}} = 130\%$ for plane strain, and $\Delta\varepsilon^c_{xx}|^{2\%}_{0.02\%} = 200\%$ for $\varepsilon^c_{xx} = \varepsilon^c_{yy}$, showing that for this material the role of the imperfection on necking formation is more important as the loading path moves away from plane strain. Note that geometric imperfections have also been shown to promote early shear band formation in shear-dominated problems in which flow localization occurs in the form of shear bands (e.g. Molinari and Clifton (1987)). Moreover, the two-zone model predictions show excellent agreement with the finite element calculations for both imperfection amplitudes, $\Delta = 0.02\%$ and 2%, and for all the loading paths investigated (like for the calculations with $\Delta = 0.2\%$ shown in previous sections of this paper). In addition, the comparison between Figs. 14a and 14b illustrates that the stability analysis predictions show better quantitative agreement with the two-zone model and the finite elements for the smaller imperfection amplitude. The decrease of Δ reduces the gradients of strain along the principal loading direction, such that the ratio between minor and major strain when the necking condition is met in the two-zone model and the unit-cell calculations comes closer to the theoretical value calculated with the stability analysis (see Appendix D). Furthermore, the hypothesis of $I^{neck} = constant$ seems to work better for a wider range of loading paths, for small imperfection amplitudes.

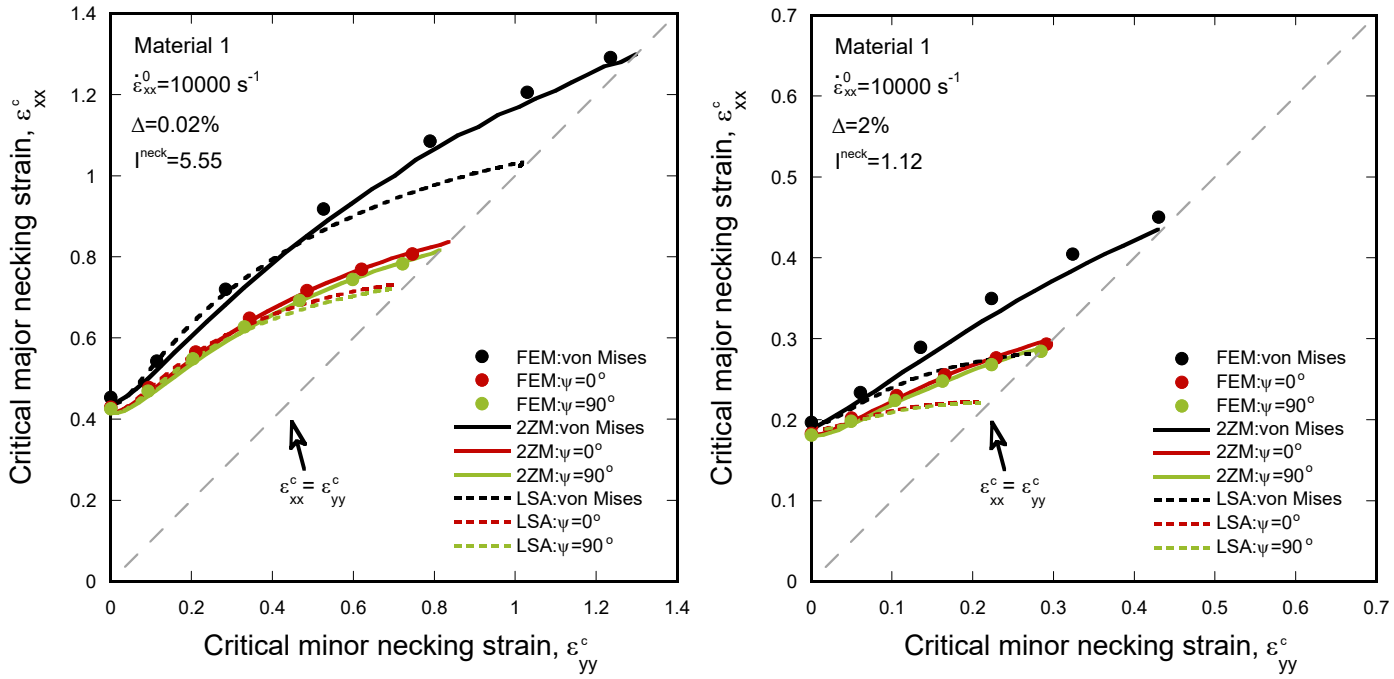

Figure 14: Comparison between finite element results (FEM), nonlinear two-zone model (2ZM) and linear stability analysis predictions (LSA). Forming limit diagram, critical major necking strain ε^c_{xx} versus critical minor necking strain ε^c_{yy}, for loading conditions ranging from $\varepsilon^c_{yy} = 0$ ($\chi = 0$, plane strain stretching) to $\varepsilon^c_{xx} = \varepsilon^c_{yy}$. The results correspond to Material 1. The two-zone model and finite element calculations correspond to two different values of the imperfection amplitude, and the stability analysis results to two different values of the cumulative instability index: (a) $\Delta = 0.02\%$ and $I^{neck} = 5.55$, and (b) $\Delta = 2\%$ and $I^{neck} = 1.12$. The cases for the material orientations $\psi = 0^\circ$ and $\psi = 90^\circ$, are compared with the corresponding isotropic von Mises material for which $F = G = H = 0.5$ and $L = M = N = 1.5$. The strain-rate sensitivity parameter is $m = 0$ (rate-independent) and the Taylor-Quinney coefficient is $\beta = 0$ (isothermal conditions of deformation). The imposed initial major strain rate is $\dot{\varepsilon}^0_{xx} = 10000$ s^{-1}.

7. Summary and concluding remarks

In this work we have developed a linear stability analysis and a nonlinear two-zone model, and have performed unit-cell finite element calculations, to investigate the effect of inertia, material strain-rate sensitivity and adiabatic heating in the formability of anisotropic metallic sheets subjected to dynamic biaxial stretching. We have investigated loading paths ranging from plane strain tension to equibiaxial tension, and a wide range of strain rates ranging from 100 s^{-1} to 50000 s^{-1}. We have studied 5 different materials whose mechanical behavior is described with an elastic isotropic, plastic anisotropic constitutive model with yielding based on Hill (1948) criterion. Materials 1 and 2 are *model materials* with elastic properties and initial density representative of steel, and anisotropy parameters and parameters of the yield stress that have been specifically tailored to heighten the effect of anisotropy in dynamic formability. Materials 3, 4 and 5 are actual materials, namely, TRIP-780 steel, aluminium alloy 5182-O and aluminium alloy 6016-T4. The finite element calculations are carried out with ABAQUS/Explicit (2016), using the unit-cell model developed by Rodríguez-Martínez et al. (2017) which includes a geometric imperfection to favor necking localization. The nonlinear two-zone model is based on the classical imperfection approach of Marciniak and Kuczyński (1967), that was recently extended by Jacques (2020) to consider inertia effects, and to include specific features to account for the hydrostatic stresses that develop inside a necked section. In this paper, the formulation of Jacques (2020), that was originally developed for isotropic plasticity criteria, is enhanced to consider anisotropic Hill (1948) materials. The stability analysis is an extension of the 2D model developed by Zaera et al. (2015) for von Mises plasticity to consider materials with yielding based on Hill (1948) criterion. Following the calibration procedure for the linear stability analysis proposed by N'souglo et al. (2020), we have determined the critical instability conditions for which a perturbation mode turns into a necking mode, which has enabled to construct forming limit diagrams with the stability analysis predictions, which are systematically compared with the two-zone model results and the finite element calculations. A key outcome of this paper is that both theoretical models predict the same trends shown by the finite element calculations for the necking strains, and they capture the effect of anisotropy in dynamic formability for the 5 materials studied. These results suggest that both nonlinear two-zone model and linear stability analysis take into account the key mechanisms which control dynamic necking localization, and that they can be used to assess the workability of metallic ductile sheets in high strain rate forming operations. Notably, the quantitative agreement between the two-zone model predictions and the finite element results is excellent for all the loading paths and strain rates investigated. On the other hand, the quantitative agreement between stability analysis predictions and finite elements depends on the amplitude of the imperfection included in the numerical model, so that the smaller the imperfection amplitude,

the better the quantitative agreement for a wider range of loading paths. The theoretical and finite element results have shown also that the effect of anisotropy on dynamic formability increases as the loading path moves away from plane strain and approaches equibiaxial tension, but it is not significantly affected by the prescribed strain rate. This indicates that it is important to account for anisotropy in the analysis and design of high energy rate forming processes. For the five materials studied, we have observed that the increase in ductility due to inertia becomes significant when the applied strain rate goes beyond $\sim 2000\ \mathrm{s}^{-1}$ (the precise value depends on the material and the plate thickness, and it is generally smaller for steels than for aluminium alloys). In addition, we have demonstrated that for large strain rates, greater than $10000\ \mathrm{s}^{-1}$ for the problem considered, inertia seems to be the main factor responsible for neck retardation, more important than the viscosity effects for the standard values of the strain-rate sensitivity exponent explored in this work. Furthermore, we have shown that, while thermal softening favors necking localization, adiabatic heating has a mild effect in the dynamic formability. In summary, this paper provides new analysis tools and specific results to build and interpret dynamic forming limit diagrams of anisotropic ductile materials. In the present study, the Hill 48 plasticity model has been employed, but the proposed methodologies can be easily extended to consider other anisotropic yield criteria. On the other hand, notice that the analysis developed in this paper is specific for ductile materials for which necking occurs before fracture. Analytical and finite element calculations impose that a neck is formed in the specimen, either including a geometric imperfection in the case of the two-zone model and the finite element calculations, or introducing a neck-like perturbation in the stability analysis. However, some authors (e.g. Makkouk et al. (2008) and Mu et al. (2020)) have shown that fracture may occur before necking in metallic materials subjected to biaxial stretching.

Acknowledgements

The research leading to these results has received funding from the European Research Council (ERC) under the European Union's Horizon 2020 research and innovation programme. Project PURPOSE, grant agreement 758056.

J.A.R.-M expresses sincere gratitude to Dr. Oana Cazacu (University of Florida, USA), Dr. Sébastien Mercier (University of Lorraine, France) and Dr. Alain Molinari (University of Lorraine, France) for many helpful discussions on anisotropic plasticity and dynamic instabilities.

Appendix A. Kinematics of the fundamental solution used in the linear stability model

We assume the following velocity field in the X direction and Y direction:

$$\begin{aligned} V_x &= \dot{\varepsilon}^0_{xx} X \\ V_y &= \dot{\varepsilon}^0_{yy} Y \end{aligned} \tag{A.1}$$

where $\dot{\varepsilon}^0_{xx}$ and $\dot{\varepsilon}^0_{yy}$ are the initial strain rates in the specimen. The displacement field, obtained by temporal integration of previous expressions, is:

$$\begin{aligned} U_x &= \dot{\varepsilon}^0_{xx} t X \\ U_y &= \dot{\varepsilon}^0_{yy} t Y \end{aligned} \tag{A.2}$$

Moreover, the Eulerian coordinates are given by:

$$\begin{aligned} x &= X + U_x = \left(1 + \dot{\varepsilon}^0_{xx} t\right) X \\ y &= Y + U_y = \left(1 + \dot{\varepsilon}^0_{yy} t\right) Y \end{aligned} \tag{A.3}$$

and the deformation rates by:

$$\begin{aligned} d_{xx} &= \frac{\partial V_x}{\partial x} = \frac{\dot{\varepsilon}^0_{xx}}{1 + \dot{\varepsilon}^0_{xx} t} \\ d_{yy} &= \frac{\partial V_y}{\partial y} = \frac{\dot{\varepsilon}^0_{yy}}{1 + \dot{\varepsilon}^0_{yy} t} \end{aligned} \tag{A.4}$$

Regarding the Z-direction, we use the incompressibility condition $d_{xx} + d_{yy} + d_{zz} = 0$ to get:

$$d_{zz} = -\left(\frac{\dot{\varepsilon}^0_{xx}}{1 + \dot{\varepsilon}^0_{xx} t} + \frac{\dot{\varepsilon}^0_{yy}}{1 + \dot{\varepsilon}^0_{yy} t} \right) \tag{A.5}$$

Therefore, we obtain:

$$\begin{aligned} V_z &= -\left(\frac{\dot{\varepsilon}^0_{xx}}{1 + \dot{\varepsilon}^0_{xx} t} + \frac{\dot{\varepsilon}^0_{yy}}{1 + \dot{\varepsilon}^0_{yy} t} \right) z \\ z &= \frac{Z}{\left(1 + \dot{\varepsilon}^0_{xx} t\right)\left(1 + \dot{\varepsilon}^0_{yy} t\right)} \\ U_z &= \left(\frac{1}{\left(1 + \dot{\varepsilon}^0_{xx} t\right)\left(1 + \dot{\varepsilon}^0_{yy} t\right)} - 1 \right) Z \end{aligned} \tag{A.6}$$

The deformation gradients are:

$$\begin{aligned} F_{xx} &= 1 + \dot{\varepsilon}^0_{xx} t \\ F_{yy} &= 1 + \dot{\varepsilon}^0_{yy} t \\ F_{zz} &= \frac{1}{\left(1 + \dot{\varepsilon}^0_{xx} t\right)\left(1 + \dot{\varepsilon}^0_{yy} t\right)} \end{aligned} \tag{A.7}$$

Appendix B. Calibration of the linear stability analysis

We have calibrated the linear stability analysis using unit-cell finite element calculations following the procedure developed by N'souglo et al. (2020). Fig. B.15 shows the evolution of the major necking strain ε^{neck}_{xx} with L^0/h^0 for the specialization of Material 1 to isotropic von Mises plasticity (obtained by imposing $F = G = H = 0.5$ and $L = M = N = 1.5$) with $m = 0$ (rate-independent material) and $\beta = 0$ (isothermal conditions of deformation). The loading path is $\chi = 0$ (plane strain stretching) and the imposed initial major strain rate is $\dot{\varepsilon}^0_{xx} = 10000$ s^{-1}. The critical major necking strain obtained in the finite element calculations (black solid markers) is 0.34 (minimum value of ε^{neck}_{xx}). We perform the linear stability analysis using this critical major necking strain as the major logarithmic strain for which the cumulative instability index is calculated. The resulting critical cumulative instability index is 3.25 (see Section 3). We take this value of I as the cumulative instability index required to trigger a neck $I^{neck} = 3.25$. Assuming that this value of I^{neck} is the same for all perturbation wavelengths, we obtain the stability analysis predictions corresponding to the dashed green curve reported in Fig. B.15 (for each value of L^0/h^0 we determine the value of the major logarithmic strain required to meet the condition $I = I^{neck}$ and this is considered to be the major necking strain).

In this paper, we take $I^{neck} = 3.25$ for $\Delta = 0.2\%$, and all the loading paths, strain rates and materials investigated. We are aware that this is a rather crude assumption, however, it enables to perform quantitative comparisons between linear stability analysis, finite element simulations and two-zone model predictions. We assume that I^{neck} depends, only, on the imperfection amplitude of the unit-cell finite element calculations used for the calibration, see Section 6.5.

For imperfection amplitudes different from $\Delta = 0.2\%$, it is necessary to re-calibrate the stability analysis. For instance, following the procedure described above, we obtain $I^{neck} = 5.55$ and 1.12 for $\Delta = 0.02\%$ and 2%, respectively (see Section 6.5). Alternatively, once I^{neck} is determined using finite elements for a given imperfection amplitude, it is also possible to obtain an estimate on the influence of Δ on the cumulative instability index relying, only, on the stability analysis, see Section 3. Considering the definition of the cumulative instability index, the

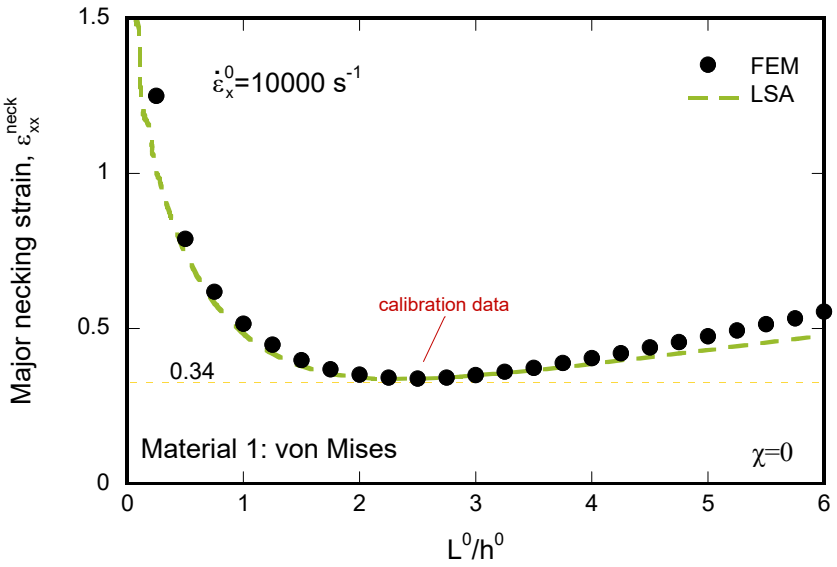

Figure B.15: Comparison between finite element results (FEM) and linear stability analysis predictions (LSA) for the specialization of Material 1 to isotropic von Mises plasticity ($F = G = H = 0.5$ and $L = M = N = 1.5$) with $m = 0$ (rate-independent) and $\beta = 0$ (isothermal conditions of deformation). Major necking strain ε_{xx}^{neck} obtained using finite element simulations (FEM) and linear stability analysis (LSA) versus L^0/h^0. Linear stability analysis results are shown for $I^{neck} = 3.25$. In the finite element simulations the amplitude of the imperfection is $\Delta = 0.2\%$. The imposed initial major strain rate is $\dot{\varepsilon}_{xx}^0 = 10000$ s^{-1}. For interpretation of the references to color in the text, the reader is referred to the web version of this article.

growth of the perturbation can be described by a relation of the form (Fressengeas and Molinari, 1994; El Maï et al., 2014):

$$A\left(t\right) = A^0 e^{I(t)} \tag{B.1}$$

with $A\left(t\right)$ being the current perturbation amplitude, A^0 the initial amplitude of the perturbation and $I\left(t\right)$ the cumulative instability index. We can identify A^0 as the initial imperfection amplitude Δ. Considering two imperfection amplitudes Δ_1 and Δ_2, and assuming that localized necking occurs when the perturbation amplitude reaches a critical value, the values of the cumulative instability index, I_1^{neck} and I_2^{neck}, associated to Δ_1 and Δ_2, are linked by the following relation:

$$I_1^{neck} - I_2^{neck} = \ln\left(\frac{\Delta_1}{\Delta_2}\right) \tag{B.2}$$

The results obtained with previous expression are in reasonable agreement with the values I^{neck} fitted from the finite element computations, see Table B.2.

Δ	I^{neck} (FEM)	I^{neck} (Eq. (B.2))
0.02%	5.55	5.553
2%	1.12	0.947

Table B.2: Comparison between the values of the cumulative instability index I^{neck} for $\Delta = 0.02\%$ and $\Delta = 2\%$ obtained with the calibration based on the unit-cell finite element calculations (FEM) and with equation (B.2).

Appendix C. Stability analysis results using an alternative calibration procedure

Fig. C.16 compares forming limit diagrams obtained with the finite element calculations, the two-zone model and the linear stability analysis, for loading cases ranging from plane strain stretching $\varepsilon^c_{yy} = 0$ (i.e. $\chi = 0$) to $\varepsilon^c_{xx} = \varepsilon^c_{yy}$. The results correspond to Material 1 and the imposed initial major strain rate is $\dot{\varepsilon}^0_{xx} = 10000\ \mathrm{s}^{-1}$. The cases for the material orientations $\psi = 0°$ and $90°$ are compared with the corresponding specialization to isotropic von Mises plasticity. The only difference with the results shown in Fig. 7 of Section 6.1 is that the linear stability analysis predictions are obtained with greater cumulative instability index $I^{neck} = 4.57$. This value has been determined following the procedure detailed in Appendix B, with the difference that the calibration of the stability analysis has been performed for $\chi = 0.5$ instead of for plane strain. As in Fig. 7, the stability analysis predictions are in qualitative agreement with the finite elements and the nonlinear two-zone model. The difference is that the quantitative agreement is worse in the vicinity of plane strain, and slightly better near $\varepsilon^c_{xx} = \varepsilon^c_{yy}$, with the stability analysis overpredicting the results derived from the finite elements and the two-zone model. However, increasing the value of the critical cumulative instability index does not change the specific effect of anisotropy on the forming limit diagram. These results indicate that the conclusions obtained in this paper with the stability analysis regarding the influence of anisotropy on dynamic formability of ductile materials are largely independent of the loading path used in the calibration procedure of the cumulative instability index.

Appendix D. Comparison of strain paths in the linear stability analysis, the two-zone model and the finite element calculations

Fig. D.17 shows the evolution of the major logarithmic strain ε_{xx} with the minor logarithmic strain ε_{yy} for the specialization to von Mises plasticity of Material 1 ($F = G = H = 0.5$ and $L = M = N = 1.5$) with $m = 0$ (rate-independent material) and $\beta = 0$ (isothermal conditions of deformation). Two different loading paths are investigated $\chi = 0.125$ and 0.5. The imposed initial major strain rate is $\dot{\varepsilon}^0_{xx} = 10000\ \mathrm{s}^{-1}$. Two normalized imperfection amplitudes, $\Delta = 0.02\%$ and 2%, are considered in the finite element calculations and in the two-zone

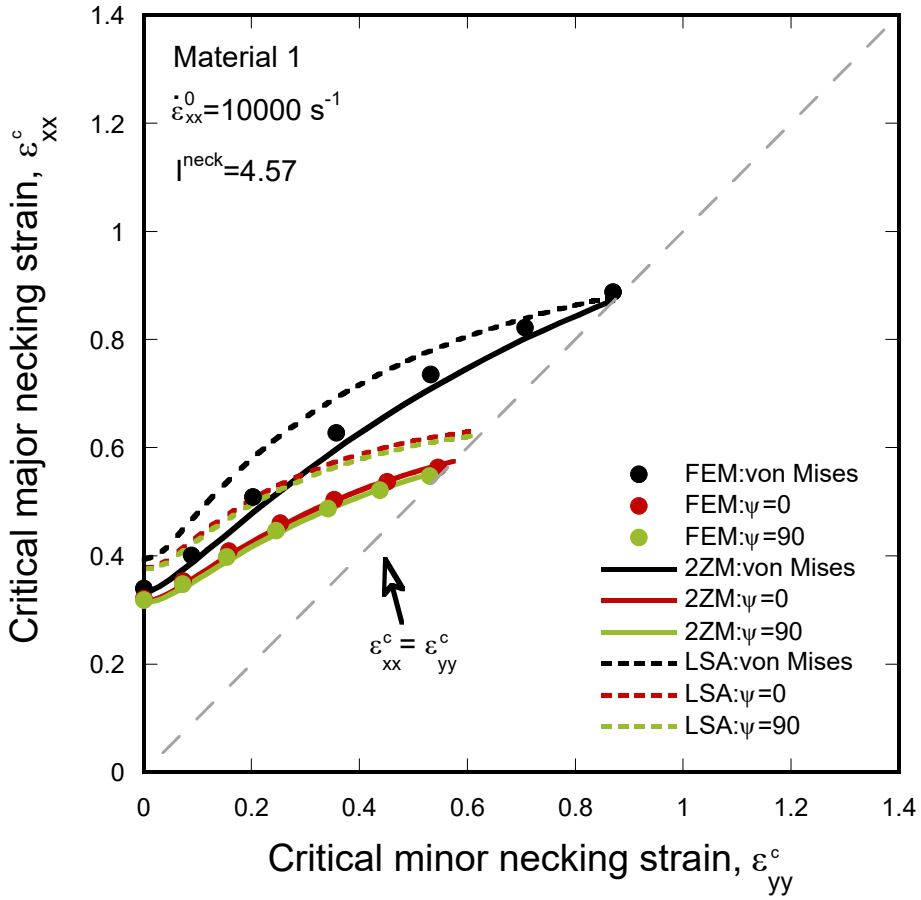

Figure C.16: Comparison between finite element results (FEM), two-zone model (2ZM) and linear stability analysis predictions (LSA) for Material 1 with $m = 0$ (rate-independent material) and $\beta = 0$ (isothermal conditions of deformation). Forming limit diagram, critical major necking strain ε^c_{xx} versus critical minor necking strain ε^c_{yy}, for loading conditions ranging from $\varepsilon^c_{yy} = 0$ ($\chi = 0$, plane strain stretching) to $\varepsilon^c_{xx} = \varepsilon^c_{yy}$. The cases for the material orientations $\psi = 0°$ and $\psi = 90°$, are compared with the corresponding isotropic von Mises material for which $F = G = H = 0.5$ and $L = M = N = 1.5$. The imposed initial major strain rate is $\dot{\varepsilon}^0_{xx} = 10000$ s^{-1}. For the finite element calculations and the two-zone model the normalized imperfection amplitude is $\Delta = 0.2\%$. In the linear stability analysis the cumulative instability index is $I^{neck} = 4.57$.

model, with the end of the $\varepsilon_{xx} - \varepsilon_{yy}$ curves corresponding to the occurrence of localized necking. For the linear stability analysis, the strain for which the necking condition is met is identified with a yellow marker, being the cumulative instability index for $\Delta = 0.02\%$ and 2%, $I^{neck} = 5.55$ and 1.12, respectively (see Section 6.5 and Appendix B).

The two-zone model shows very good agreement with the finite element calculations for the two imperfection amplitudes and both loading paths. As the loading starts, the $\varepsilon_{xx} - \varepsilon_{yy}$ curves obtained with the two-zone model and the finite elements coincide with the fundamental solution corresponding to the stability analysis (green dashed curve). With the continuation of the deformation process, the results deviate from the fundamental solution – because the imperfection leads to the development of strain gradients along the principal loading direction of the specimen– with decreasing slope which tends to zero when the necking is fully formed. Hence, the ratio between minor and major strain when necking occurs is greater than the theoretical value corresponding to the stability analysis (the relation between ε_{xx} and ε_{yy} when necking occurs for the finite element calculations is indicated in the plots). Furthermore, the increase of the imperfection amplitude causes that the two-zone model and the finite elements deviate earlier from the fundamental solution, and that the ratio between minor and major strains when necking occurs moves further away from the theoretical value. In addition, notice that the necking condition in the stability analysis is attained for lower values of ε_{xx} and ε_{yy} than in the two-zone model and in the finite element calculations. The greater relative differences –relative to the absolute values of ε_{xx} and ε_{yy}– correspond to $\chi = 0.5$ and $\Delta = 2\%$. This explains that the stability analysis underestimates the forming limit diagrams calculated with the two-zone model and the finite elements in Section 6, with increasing differences as the loading path moves away from plane strain and as the imperfection amplitude increases.

References

ABAQUS/Explicit, 2016. Abaqus Explicit v6.16 User's Manual. version 6.16 ed., ABAQUS Inc., Richmond, USA.

Alves Zapata, J.R., 2016. Magnetic pulse forming processes: Computational modelling and experiemental validation. Ph.D. thesis. MINES ParisTech.

Aretz, H., Barlat, F., 2013. New convex yield functions for orthotropic metal plasticity. International Journal of Non-Linear Mechanics 51, 97 – 111.

Audoly, B., Hutchinson, J.W., 2016. Analysis of necking based on a one-dimensional model. Journal of the Mechanics and Physics of Solids 97, 68 – 91. SI:Pierre Suquet Symposium.

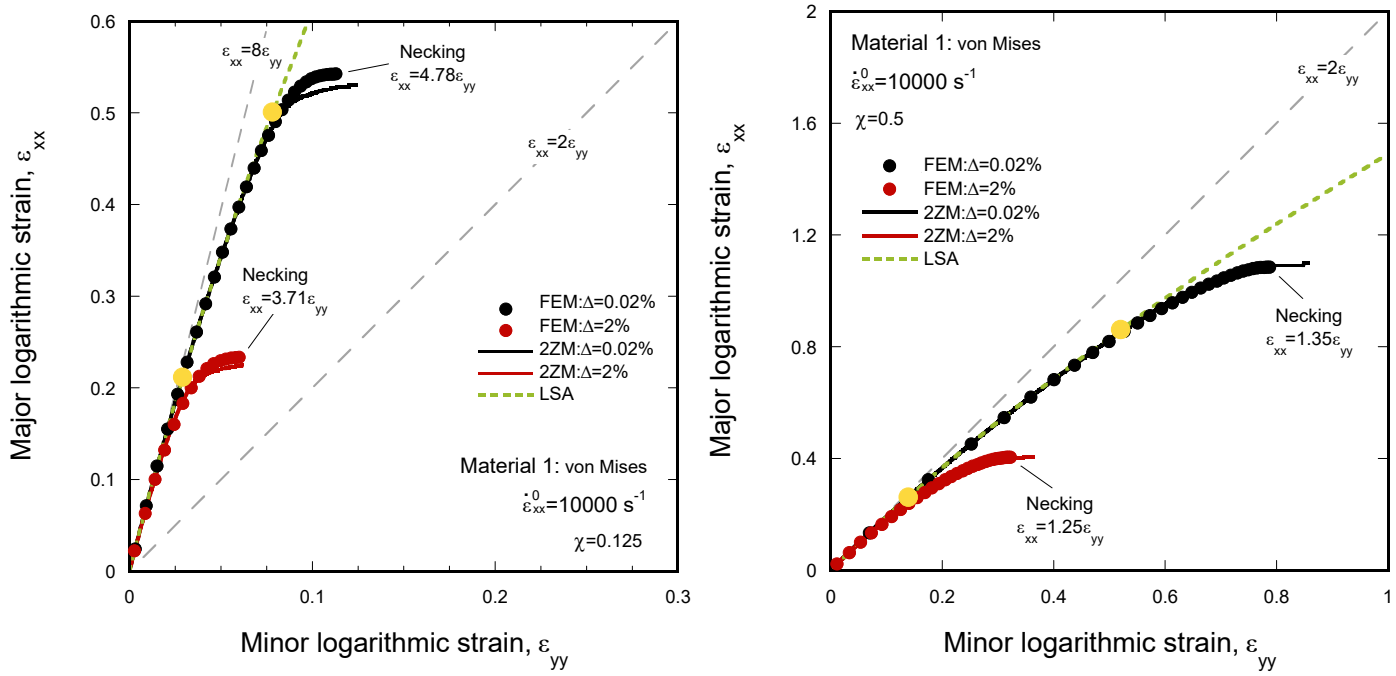

(a) (b)

Figure D.17: Comparison between finite element results (FEM), nonlinear two-zone model (2ZM) and linear stability analysis predictions (LSA). Evolution of the major logarithmic strain ε_{xx} with the minor logarithmic strain ε_{yy} for the specialization to von Mises plasticity of Material 1 ($F = G = H = 0.5$ and $L = M = N = 1.5$) with $m = 0$ (rate-independent material) and $\beta = 0$ (isothermal conditions of deformation). The imposed initial major strain rate is $\dot{\varepsilon}^0_{xx} = 10000\ \mathrm{s}^{-1}$. For the finite element calculations and the two-zone model, two normalized imperfection amplitudes are considered $\Delta = 0.02\%$ and 2%. The last data of the $\varepsilon_{xx} - \varepsilon_{yy}$ curves obtained with the two-zone model and the unit-cell calculations corresponds to the necking formation. For the linear stability analysis, the necking formation is identified with a yellow marker. For $\Delta = 0.02\%$ the cumulative instability index is $I^{neck} = 5.55$, and for $\Delta = 2\%$ is $I^{neck} = 1.12$. Two different loading paths are considered: (a) $\chi = 0.125$ and (b) $\chi = 0.5$. For interpretation of the references to color in the text, the reader is referred to the web version of this article.

Audoly, B., Hutchinson, J.W., 2019. One-dimensional modeling of necking in rate-dependent materials. Journal of the Mechanics and Physics of Solids 123, 149 – 171. The N.A. Fleck 60th Anniversary Volume.

Balanethiram, V.S., Daehn, G.S., 1992. Enhanced formability of interstitial free iron at high strain rates. Scripta Metallurgica et Materialia 27, 1783 – 1788.

Balanethiram, V.S., Daehn, G.S., 1994. Hyperplasticity: Increased forming limits at high workpiece velocity. Scripta Metallurgica et Materialia 30, 515 – 520.

Banabic, D., , Siegert, K., 2004. Anisotropy and formability of AA5182-0 aluminium alloy sheets. CIRP Annals 53, 219–222.

Banabic, D., 2010. Sheet Metal Forming Processes: Constitutive Modelling and Numerical Simulation. 1 ed., Springer Science & Business Media, Berlin.

Banabic, D., Barlat, F., Cazacu, O., Kuwabara, T., 2010. Advances in anisotropy and formability. International Journal of Material Forming 3, 165–189.

Baral, M., Hama, T., Knudsen, E., Korkolis, Y.P., 2018. Plastic deformation of commercially-pure titanium: experiments and modeling. International Journal of Plasticity 105, 164 – 194.

Bridgman, P.W., 1952. Studies in large plastic flow and fracture, with special emphasis on the effects of hydrostatic pressure, vol.1. McGraw-Hill Book Company, Inc., New York.

Bron, F., Besson, J., 2004. A yield function for anisotropic materials application to aluminum alloys. International Journal of Plasticity 20, 937 – 963.

Brunet, M., Morestin, F., 2001. Experimental and analytical necking studies of anisotropic sheet metals. Journal of Materials Processing Technology 112, 214 – 226.

Børvik, T., Hopperstad, O., Berstad, T., Langseth, M., 2001. A computational model of viscoplasticity and ductile damage for impact and penetration. European Journal of Mechanics - A/Solids 20, 685 – 712.

Butuc, M., Rocha, A., Duarte, J., Barlat, F., Grácio, J., 2002. Forming limit diagram for 6016-T4 aluminium alloy deformed along linear and complex strain paths. Key Engineering Materials 230, 529–532.

Butuc, M.C., Gracio, J.J., Da Rocha, A.B., 2003. A theoretical study on forming limit diagrams prediction. Journal of Materials Processing Technology 142, 714–724.

Cazacu, O., Plunkett, B., Barlat, F., 2006. Orthotropic yield criterion for hexagonal closed packed metals. International Journal of Plasticity 22, 1171–1194.

Cazacu, O., Rodríguez-Martínez, J.A., 2019. Effects of plastic anisotropy on localization in orthotropic materials: New explicit expressions for the orientation of localization bands in flat specimens subjected to uniaxial tension. Journal of the Mechanics and Physics of Solids 126, 272 – 284.

Choi, K., Soulami, A., Liu, W., Sun, X., Khaleel, M., 2010. Influence of various material design parameters on deformation behaviors of trip steels. Computational Materials Science 50, 720 – 730.

Considère, A., 1885. Mémoire sur l'emploi du fer et de l'acier dans les constructions. Ann. Ponts et Chaussées 9, 574–775.

Czarnota, C., Molinari, A., Mercier, S., 2017. The structure of steady shock waves in porous metals. Journal of the Mechanics and Physics of Solids 107, 204–228.

Daehn, G.S., Altynova, M., Balanethiram, V.S., Fenton, G., Padmanabhan, M., Tamhane, A., Winnard, E., 1995. High-velocity metal forming — an old technology addresses new problems. The Journal of The Minerals, Metals and Materials Society 47, 42 – 45.

Dariani, B.M., Liaghat, G.H., Gerdooei, M., 2009. Experimental investigation of sheet metal formability under various strain rates. Proceedings of the Institution of Mechanical Engineers, Part B: Journal of Engineering Manufacture 223, 703–712.

Dasappa, P., Inal, K., Mishra, R., 2012. The effects of anisotropic yield functions and their material parameters on prediction of forming limit diagrams. International Journal of Solids and Structures 49, 3528 – 3550. New Challenges in Mechanics & Materials for Sheet Metal Forming.

Dey, S., Børvik, T., Hopperstad, O., Leinum, J., Langseth, M., 2004. The effect of target strength on the perforation of steel plates using three different projectile nose shapes. International Journal of Impact Engineering 30, 1005 – 1038. Eighth International Symposium on Plasticity and Impact Mechanics (IMPLAST 2003).

Dudzinski, D., Molinari, A., 1991. Perturbation analysis of thermoviscoplastic instabilities in biaxial loading. International Journal of Solids and Structures 27, 601–628.

El Maï, S., Mercier, S., Petit, J., Molinari, A., 2014. An extension of the linear stability analysis for the prediction

of multiple necking during dynamic extension of round bar. International Journal of Solids and Structures 51, 3491–3507.

Fressengeas, C., Molinari, A., 1985. Inertia and thermal effects on the localization of plastic flow. Acta Metallurgica 33, 387–396.

Fressengeas, C., Molinari, A., 1994. Fragmentation of rapidly stretching sheets. European Journal of Mechanics A/Solids 13, 251–268.

Friedman, P.A., Pan, J., 2000. Effects of plastic anisotropy and yield criteria on prediction of forming limit curves. International Journal of Mechanical Sciences 42, 29 – 48.

Gayakwad, D., Dargar, M.K., Sharma, P.K., Purohit, R., Rana, R.S., 2014. A review on electromagnetic forming process. Procedia Materials Science 6, 520 – 527. 3rd International Conference on Materials Processing and Characterisation (ICMPC 2014).

Golovashchenko, S.F., 2007. Material formability and coil design in electromagnetic forming. Journal of Materials Engineering and Performance 16, 314–320.

Golovashchenko, S.F., Gillard, A.J., Mamutov, A.V., 2013. Formability of dual phase steels in electrohydraulic forming. Journal of Materials Processing Technology 213, 1191 – 1212.

Graf, A., Hosford, W., 1990. Calculations of forming limit diagrams. Metallurgical Transactions A 21, 87–93.

Greco, F., Deckers, E., Stroobants, J., Van Poppel, S., Linck, K., Desmet, W., 2018. Finite element simulation of the dynamic behaviour of deep drawn components with accurate thickness description. Finite Elements in Analysis and Design 138, 12 – 20.

Hill, R., 1948. A theory of the yielding and plastic flow of anisotropic metals, in: Proceedings of the Royal Society of London A: Mathematical, Physical and Engineering Sciences, The Royal Society. pp. 281–297.

Hill, R., 1952. On discontinous plastic states, with special reference to localized necking in thin sheets. Journal of the Mechanics and Physics of Solids 1, 19–30.

Hu, W., 2007. A novel quadratic yield model to describe the feature of multi-yield-surface of rolled sheet metals. International Journal of Plasticity 23, 2004 – 2028.

Huh, J., Huh, H., Lee, C.S., 2013. Effect of strain rate on plastic anisotropy of advanced high strength steel sheets. International Journal of Plasticity 44, 23 – 46.

Hutchinson, J.W., Neale, K., 1977. Influence of strain rate sensitivity on necking under uniaxial tension. Acta Metallurgica 25, 839–846.

Hutchinson, J.W., Neale, K.W., Needleman, A., 1978a. Sheet necking-III. Strain-rate effects. Springer, Boston, MA. In Mechanics of sheet metal forming, pp. 269–285.

Hutchinson, J.W., Neale, K.W., Needleman, A., 1978b. Sheet necking—I. Validity of plane stress assumptions of the long-wavelength approximation. Springer, Boston, MA. In Mechanics of sheet metal forming, pp. 111–126.

Iwamoto, T., Tsuta, T., Tomita, Y., 1998. Investigation on deformation mode dependence of strain-induced martensitic transformation in trip steels and modelling of transformation kinetics. International Journal of Mechanical Sciences 40, 173 – 182.

Jacques, N., 2020. An analytical model for necking strains in stretched plates under dynamic biaxial loading. International Journal of Solids and Structures 200-201, 198 – 212.

Jacques, N., Mercier, S., Molinari, A., 2012. Effects of microscale inertia on dynamic ductile crack growth. Journal of the Mechanics and Physics of Solids 60, 665–690.

Ju, L., Patil, S., Dykeman, J., Altan, T., 2015. Forming of Al 5182-O in a servo press at room and elevated temperatures. Journal of Manufacturing Science and Engineering 137.

Karafillis, A.P., Boyce, M.C., 1993. A general anisotropic yield criterion using bounds and a transformation weighting tensor. Journal of the Mechanics and Physics of Solids 41, 1859 – 1886.

Korkolis, Y.P., Mitchell, B.R., Locke, M.R., Kinsey, B.L., 2018. Plastic flow and anisotropy of a low-carbon steel over a range of strain-rates. International Journal of Impact Engineering 121, 157 – 171.

Koubaa, S., Mars, J., Wali, M., Dammak, F., 2017. Numerical study of anisotropic behavior of aluminum alloy subjected to dynamic perforation. International Journal of Impact Engineering 101, 105 – 114.

Kuroda, M., Tvergaard, V., 2000. Forming limit diagrams for anisotropic metal sheets with different yield criteria. International Journal of Solids and Structures 37, 5037–5059.

Li, B., Nye, T.J., Wu, P.D., 2010. Predicting the forming limit diagram of AA 5182-O. The Journal of Strain Analysis for Engineering Design 45, 255–273.

Makkouk, R., Bourgeois, N., Serri, J., Bolle, B., Martiny, M., Teaca, M., Ferron, G., 2008. Experimental and theoretical analysis of the limits to ductility of type 304 stainless steel sheet. European Journal of Mechanics - A/Solids 27, 181 – 194.

Mamalis, A.G., Manolakos, D.E., Kladas, A.G., Koumoutsos, A.K., 2004. Electromagnetic forming and powder processing: Trends and developments. Applied Mechanics Reviews 57, 299–324.

Marciniak, Z., Kuczyński, K., 1967. Limit strains in the process of stretch-forming sheet metal. International Journal of Mechanical Sciences 9, 609–620.

Mercier, S., Granier, N., Molinari, A., Llorca, F., Buy, F., 2010. Multiple necking during the dynamic expansion of hemispherical metallic shells, from experiments to modelling. Journal of the Mechanics and Physics of Solids 58, 955–982.

Mises, R.V., 1928. Mechanik der plastischen formänderung von kristallen. ZAMM - Journal of Applied Mathematics and Mechanics / Zeitschrift für Angewandte Mathematik und Mechanik 8, 161–185.

Molinari, A., Clifton, R., 1987. Analytical characterization of shear localization in themoviscoplastic materials. Journal of Applied Mechanics 54, 806–812.

Mu, L., Jia, Z., Ma, Z., Shen, F., Sun, Y., Zang, Y., 2020. A theoretical prediction framework for the construction of a fracture forming limit curve accounting for fracture pattern transition. International Journal of Plasticity 129, 102706.

Needleman, A., 1988. Material rate dependence and mesh sensitivity in localization problems. Computer Methods in Applied Mechanics and Engineering 67, 69–85.

Nemat-Nasser, S., Li, Y., 1998. Flow stress of f.c.c. polycrystals with application to OFHC Cu. Acta Materialia 46, 565 – 577.

N'souglo, K.E., Rodríguez-Martínez, J.A., Cazacu, O., 2020. The effect of tension-compression asymmetry on the formation of dynamic necking instabilities under plane strain stretching. International Journal of Plasticity 128, 102656.

Padmanabhan, R., Oliveira, M.C., Baptista, A.J., Alves, J.L., Menezes, L.F., 2009. Numerical study on the influence of initial anisotropy on optimal blank shape. Finite Elements in Analysis and Design 45, 71 – 80.

Panich, S., Barlat, F., Uthaisangsuk, V., Suranuntchai, S., Jirathearanat, S., 2013. Experimental and theoretical formability analysis using strain and stress based forming limit diagram for advanced high strength steels. Materials & Design 51, 756–766.

Park, J.M., Moon, J., Bae, J.W., Jang, M.J., Park, J., Lee, S., Kim, H.S., 2018. Strain rate effects of dynamic compressive deformation on mechanical properties and microstructure of cocrfemnni high-entropy alloy. Materials Science and Engineering: A 719, 155 – 163.

Parmar, A., Mellor, P., 1978. Predictions of limit strains in sheet metal using a more general yield criterion. International Journal of Mechanical Sciences 20, 385 – 391.

Rodríguez-Martínez, J.A., Molinari, A., Zaera, R., Vadillo, G., Fernández-Sáez, J., 2017. The critical neck spacing in ductile plates subjected to dynamic biaxial loading: on the interplay between loading path and inertia effects. International Journal of Solids and Structures 108, 74–84.

Rohatgi, A., Soulami, A., Stephens, E.V., Davies, R.W., Smith, M.T., 2014. An investigation of enhanced formability in AA5182-O al during high-rate free-forming at room-temperature: Quantification of deformation history. Journal of Materials Processing Technology 214, 722 – 732.

Rusinek, A., Klepaczko, J.R., 2001. Shear testing of a sheet steel at wide range of strain rates and a constitutive relation with strain-rate and temperature dependence of the flow stress. International Journal of Plasticity 17, 87 – 115.

Seth, M., Vohnout, V.J., Daehn, G.S., 2005. Formability of steel sheet in high velocity impact. Journal of Materials Processing Technology 168, 390 – 400.

Shen, F., Münstermann, S., Lian, J., 2019. Forming limit prediction by the marciniak–kuczynski model coupled with the evolving non-associated hill48 plasticity model. Journal of Materials Processing Technology , 116384.

Song, F.M., Zhang, X., Wang, Z.R., Yu, L.Z., 2004. A study of tube electromagnetic forming. Journal of Materials Processing Technology 151, 372 – 375. Special Volume dedicated to Professor Z.R. Wang on the occasion of his 70th Birthday.

Sowerby, R., Duncan, J.L., 1971. Failure in sheet metal in biaxial tension. International Journal of Mechanical Sciences 13, 217 – 229.

Tomita, Y., Iwamoto, T., 1995. Constitutive modeling of trip steel and its application to the improvement of mechanical properties. International Journal of Mechanical Sciences 37, 1295 – 1305.

Vaz-Romero, A., Rodríguez-Martínez, J.A., Mercier, S., Molinari, A., 2017. Multiple necking pattern in nonlinear elastic bars subjected to dynamic stretching: The role of defects and inertia. International Journal of Solids and Structures 125, 232 – 243.

Wood, W.W., 1967. Experimental mechanics at velocity extremes - very high strain rates. Experimental Mechanics 7, 441 – 446.

Xavier, M., Czarnota, C., Jouve, D., Mercier, S., Dequiedt, J.L., Molinari, A., 2020. Extension of linear stability analysis for the dynamic stretching of plates: Spatio-temporal evolution of the perturbation. European Journal of Mechanics - A/Solids 79, 103860.

Xue, Z., Vaziri, A., Hutchinson, J.W., 2008. Material aspects of dynamic neck retardation. Journal of the Mechanics and Physics of Solids 56, 93–113.

Zaera, R., Fernández-Sáez, J., 2006. An implicit consistent algorithm for the integration of thermoviscoplastic constitutive equations in adiabatic conditions and finite deformations. International Journal of Solids and Structures 43, 1594–1612.

Zaera, R., Rodríguez-Martínez, J.A., Vadillo, G., Fernández-Sáez, J., Molinari, A., 2015. Collective behaviour and spacing of necks in ductile plates subjected to dynamic biaxial loading. Journal of the Mechanics and Physics of Solids 85, 245–269.

Zerilli, F.J., Armstrong, R.W., 1987. Dislocation-mechanics-based constitutive relations for material dynamics calculations. Journal of Applied Physics 61, 1816–1825.

Zheng, X., N'souglo, K.E., Rodríguez-Martínez, J.A., Srivastava, A., 2020. Dynamics of necking and fracture in ductile porous materials. Journal of Applied Mechanics 87.

Zhou, C., Zhang, W.T., Zhang, S.J., Deng, J.J., Xia, Q.X., 2018. Effect of strain path change on formability of TRIP steels, in: Technology of Plasticity, Trans Tech Publications Ltd. pp. 223–229.

Zhou, F., Molinari, J.F., Ramesh, K.T., 2006. An elasto-visco-plastic analysis of ductile expanding ring. International Journal of Impact Engineering 33, 880–891.